JOURNAL OF GEOPHYSICAL RESEARCH, VOL. 115, B07411, doi:10.1029/2009JB006599, 2010

Coseismic and postseismic slip from the 2003 San Simeon earthquake and their effects on backthrust slip and the 2004 Parkfield earthquake

I. A. Johanson[1] and R. Bürgmann[1]

Received 8 May 2009; revised 4 January 2010; accepted 25 February 2010; published 20 July 2010.

[1] The 2003 M6.5 San Simeon earthquake occurred less than a year before and 50 km west of the long-awaited Parkfield earthquake of 2004. Aftershocks of the San Simeon event occurred not only on the presumptive rupture plane but also delineated subconjugate structures to the east (backthrusts). InSAR data show a complex pattern of deformation during the postseismic time interval and suggest that shallow postseismic slip may have occurred on the backthrust structures. In this paper we present a model inversion for slip during and after the earthquake from four interferograms and GPS data. We find that the data are well-fit when coseismic slip is allowed on two planes, the main rupture plane and a backthrust structure to the south. The backthrust structure accommodates slip amounting to about one third of the coseismic moment release. Shallow postseismic slip also occurred on the main rupture plane, updip from the coseismic slip, and on the southern backthrust. Postseismic slip on the more northern backthrust structure is not well-constrained and the data is fit nearly as well without including it. The areas of postseismic slip on the backthrusts correspond well with areas that experienced unclamping and little slip is found in regions of clamping. No value for the coefficient of friction below 1.0 results in a Coulomb Failure Stress field that matches the aseismic slip distributions better than the normal stress alone. We also investigate whether static stress changes from the San Simeon earthquake acted to encourage right-lateral strike slip on the Parkfield segment of the San Andreas fault. We find that the San Simeon earthquake's rupture planes were oriented in such a way that the maximum increase in Coulomb failure stress on the San Andreas fault occurred on the Parkfield segment. The 2004 Parkfield earthquake differed from its expected behavior by nucleating in the southern portion of the Parkfield segment; an area that experienced increased shear stress of 0.1–0.14 bars from coseismic slip in the San Simeon earthquake. Postseismic slip from San Simeon further loaded the southern portion of the Parkfield segment preferentially over the northern portion, though the size of the stress changes was small (0.03–0.04 bars).

Citation: Johanson, I. A., and R. Bürgmann (2010), Coseismic and postseismic slip from the 2003 San Simeon earthquake and their effects on backthrust slip and the 2004 Parkfield earthquake, *J. Geophys. Res.*, *115*, B07411, doi:10.1029/2009JB006599.

1. Introduction

[2] The M6.5 San Simeon earthquake (SSEQ) of 22 December 2003 occurred less than a year before the 2004 Parkfield earthquake (PKEQ), the long-awaited fulfillment of the Parkfield Earthquake Prediction Experiment. In this paper we investigate whether stress changes from either the coseismic or postseismic time intervals of the SSEQ acted to encourage the PKEQ's occurrence. We also investigate how coseismic stress changes may have influenced SSEQ postseismic afterslip. Although it had a small equivalent moment (14% of coseismic), the postseismic slip distribution appears to have been quite complex, involving slip on several back thrust structures.

[3] The SSEQ was a thrust event in the Central California Coast Range, ~50 km west of the Parkfield segment [*Hardebeck et al.*, 2004]. The earthquake is attributed to the northeast-dipping Oceanic fault (Figure 1), although no surface rupture was reported to confirm this as the responsible structure [*Hardebeck et al.*, 2004]. Aftershocks occurred mostly within the apparent hanging wall block and while they tend to encircle the rupture area on the northeast dipping plane, they also appear to delineate as many as five separate subconjugate (backthrust) structures [*Hauksson et al.*, 2004; *McLaren et al.*, 2008].

[4] The Oceanic fault forms the northern boundary of the Los Osos domain, a region of alternating NE and SW dipping

[1]Berkeley Seismological Laboratory, University of California, Berkeley, California, USA.

0148-0227/10/2009JB006599

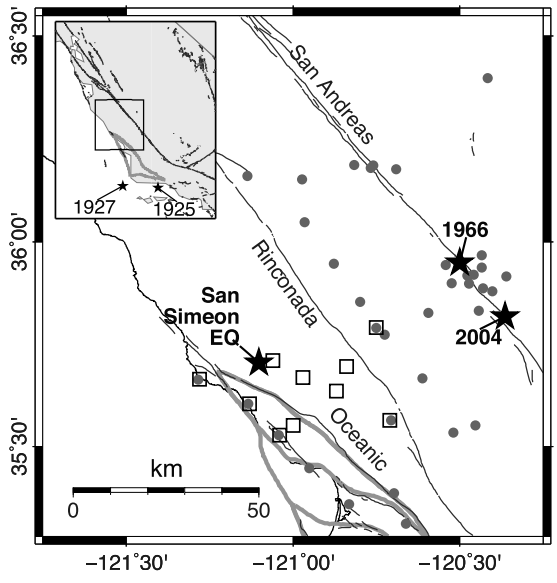

Figure 1. Location map of study area showing Global Positioning System (GPS) stations used in this study. Grey circles are sites with coseismic offsets determined by *Rolandone et al.* [2006]. Squares are GPS sites with postseismic data used to estimate the decay time constant for our model. Epicenters of the 1966 and 2004 Parkfield and San Simeon earthquakes are shown by stars. Thick grey lines in both maps are the outlines the Los Osos domain [*Lettis et al.*, 2004]. Inset map shows study area location (black square) relative to the California coastline and the locations of the 1927 M7.0 Lompoc and 1925 M6.2 Santa Barbara earthquakes.

structures bounded by the Transverse Ranges to the south and the Hosgri fault zone to the west (Figure 1). The amount of distributed dextral slip attributed to this region has been quite variable, though more recent estimates suggest 4–6 mm/yr of Pacific-North America relative motion is accommodated by Los Osos domain faults including the Hosgri fault [*Shen and Jackson*, 1993; *Feigl et al.*, 1993; *Lettis et al.*, 2004]. The domain is sandwiched between the clockwise-rotating Transverse Ranges and stable units to the north and east, with distributed deformation on oblique-thrust faults in its interior [*Lettis et al.*, 2004]. Thus significant plate-boundary perpendicular contraction is not necessary to produce the observed oblique-thrust motions on Los Osos domain faults, which trend more northwesterly than the San Andreas fault. Contraction across the domain, oriented in a northeast-southwest direction, occurs at quite low rates. *Rolandone et al.* [2008] resolved contraction across the Coast Ranges at a rate of 1–4.5 mm/yr, using a set of 42 GPS velocities spanning across the Central San Andreas fault region and into the Coast Ranges, likewise *Lettis et al.* [2004] prefer <2 mm/yr.

[5] No other similarly-sized earthquakes have been recorded in the Los Osos domain. Although the 1927 M7.0 Lompoc and 1925 M6.2 Santa Barbara earthquakes occurred offshore and to the south (Figure 1). These were similar to the San Simeon earthquake in that they were both thrust mechanism events with northwest-striking rupture planes and likely occurred in response to the complex strain field produced by rotation of the Transverse Ranges [*Helmberger et al.*, 1992; *Toppozada et al.*, 1978].

1.1. Parkfield Earthquake of 2004

[6] A series of M~6 earthquakes near the town of Parkfield and with a recurrence interval of ~22 years, prompted *Bakun and Lindh* [1985] to predict that the next M6 earthquake would occur in 1988. The Parkfield segment became one of the best-instrumented fault segments in the United States and though the 2004 earthquake occurred ~16 years "late," it has provided valuable insight into earthquake processes [e.g., *Bakun et al.*, 2005].

[7] Not only did the past Parkfield earthquakes occur with quasi-regularity but their rupture patterns also shared several characteristics. Analysis of the seismograms from the 1922, 1934, and 1966 earthquakes suggested that they all had hypocenters near Middle Mountain (Figure 1) and propagated to the southeast along the San Andreas fault [*Bakun and McEvilly*, 1979, 1984].

[8] The Parkfield Prediction Experiment was thereby a test of the characteristic earthquake model, as well as a test of the time-predictable model. The 2004 Parkfield earthquake was similar to the past events in that the coseismic rupture had a moment magnitude near M6.0 and peak slip ~10 km south of Middle Mountain [*Johanson et al.*, 2006; *Murray et al.*, 2006]. However, it differed from the characteristic pattern established by the 1922–1966 Parkfield earthquakes in that its hypocenter was located south of the town of Parkfield and rupture propagated northwest [*Langbein et al.*, 2005].

1.2. Coulomb Stress and Earthquakes

[9] Several hypotheses have been proposed for why the Parkfield earthquake was delayed by 16 years relative to the original prediction. These include lengthening of the recurrence interval due to viscous relaxation of the crust following the 1857 Fort Tejon earthquake [*Ben-Zion et al.*, 1993] and decreased stress on the Parkfield segment from the 1983 Coalinga-Nuñez earthquakes [*Toda and Stein*, 2002]. From 1993 to 1996 a fault slip transient on the San Andreas fault occurred that may have also released stress on the Parkfield segment near the nucleation site of the 1966 Parkfield earthquake [*Gwyther et al.*, 1996; *Murray and Segall*, 2005]. None of these can account for the entire 16 years of delay, though they may have acted in combination. Nonetheless, by 2004 the Parkfield segment was clearly due to produce its next earthquake; even a small increment of stress on the fault plane could have triggered the 2004 earthquake if the segment was very close to failure.

[10] While stress changes as low as 0.1–0.2 bars have been observed to correlate with the locations of aftershocks [*King et al.*, 1994; *Hardebeck et al.*, 1998; *Toda et al.*, 1998], small stress changes are also associated with the sites of future large main shock hypocenters. *Stein et al.* [1997] studied a sequence of 10 M ≥ 6.7 earthquakes spanning 53 years on the North Anatolian Fault in Turkey and found that all but one correlated with Coulomb stress increases between 1 and 10 bars from prior events. *Harris and Simpson* [2002] compared stress changes produced by several models of the 1992 M7.3 Landers earthquake and found that under most scenarios, rupture was discouraged at the site of the 1999 M7.1 Hector Mine earthquake hypocenter, and after including stress changes from the 1992 Pisgah aftershock, they found that the CFS increase at the Hector Mine hypocenter was no more than 3 bars.

[11] Stress changes have also been found to correspond with areas of high slip in future earthquakes. Similar to other authors, *Parsons and Dreger* [2000] found that the Landers earthquake did not increase the CFS at the Hector Mine hypocenter by much (0.5 bars); however, they found that peak slip in the Hector Mine earthquake correlated with increased CFS in the range 0.5–1.5 bars. *Perfettini et al.* [1999] also noted that the hypocentral region of the 1989 M6.9 Loma Prieta earthquake was not brought closer to failure by two M5.3–5.4 foreshocks but that unclamping from these events corresponded to areas of significant slip during the main shock.

[12] Postseismic processes have also been implicated in earthquake triggering. Postseismic afterslip from the 1999 Izmit earthquake nearly doubled the input stress at the hypocenter of the Düzce earthquake, which occurred 87 days later [*Hearn et al.*, 2002]. The effect of stress changes from postseismic afterslip or viscous relaxation can also help explain the delay of months to years for some triggered earthquakes [*Freed and Jin*, 2001; *Pollitz and Sacks*, 2002; *Price and Burgmann*, 2002].

[13] In this study, we use space geodetic data to develop a slip model for the 2003 SSEQ. We calculate the static stress changes along the San Andreas fault produced in both the coseismic and postseismic periods of the SSEQ and investigate whether they promoted the 2004 Parkfield earthquake, influenced the slip distribution, and/or contributed to the change in hypocenter location from that of the previous Parkfield earthquakes. We begin by performing a search for the optimal orientation of the rupture plane, which is then discretized and used in a simultaneous inversion for coseismic and postseismic slip. We test several scenarios, including coseismic and/or postseismic slip on backthrust structures, to find our preferred slip model. The preferred model is used to calculate the static stress change fields and their impact on SSEQ aftershock occurrence, SSEQ afterslip, and the Parkfield segment.

2. Data

2.1. InSAR

[14] We use four interferograms: two from the European Space Agency's (ESA's) Envisat satellite (beam 2), one from ESA's ERS-2 satellite, and the fourth from the Canadian Space Agency's RADARSAT-1 (RSAT, Table 2). Interferograms are formed from the difference in phase of a scattered radar pulse from satellite acquisitions on two separate occasions. The phase difference is proportional to the change in distance between the ground and the satellite between the two acquisition dates (range change) and thus provides a measure of ground deformation in the satellite's look direction (see *Bürgmann et al.* [2000] for more details). The look direction is defined by the satellite's heading and the look angle, which is the angle off-vertical that the satellite views the ground. All four interferograms have have steep look angles (Table 2) so that vertical motions map into range change more strongly than horizontal.

[15] Two of the interferograms used here span only the postseismic time interval following the SSEQ (interferograms C and D) and two are mixed, spanning both the coseismic and portions of the postseismic periods (interferograms A and B). Because they have different look directions, the fringe patterns in Interferograms A and B are not the same. Vertical motions affect the range change measurement identically; therefore differences between the two are an indication of horizontal motion. For example, interferogram B has more dense fringing south of the SSEQ epicenter than A. Eastward motion and subsidence both cause an increase in range change for the ascending mode interferogram B, but for descending mode interferogram A, eastward motion causes range change decrease and acts to partially cancel out the range change increase produced by subsidence.

[16] Despite being from different satellites and having different look directions, both A and B contain a large decorrelated patch over the center of the deforming area. Decorrelation noise looks like speckle and can be caused by large perpendicular baselines and exacerbated by steep topography. Though the decorrelated area is over the Coast Ranges, these are not so steep that they prevent correlation in C or D. Decorrelation can also be related to large amounts of deformation that cause aliasing of the signal as the fringe density approaches the pixel spacing. While high fringe rates can be seen on the northern border of the decorrelated areas in A and B, their other edges are not bordered by the same density of fringing. While no single cause seems to explain the decorrelation, some combination of topography and strain may be responsible for producing the similar decorrelation patterns in two interferograms.

[17] Interferograms C and D span early and later portions of the postseismic period respectively. Interferogram C is identical to that presented by *McLaren et al.* [2008] and shows evidence for slip on at least two backthrust structures (Figure 2c). A compact and linear fringe to the south indicates near surface movement on a subparallel structure to the Oceanic fault (labeled G in Figure 2c). While interferogram D has sparser data coverage, it also contains some indication of motion in this area. To the north in C, a linear fringe gives way to a broader lobe of deformation in the area of the earthquake's epicenter. Interferogram D shows no similar lobe or dense fringing in the same area, it shows only a region of deformation trending along the Oceanic fault

[18] A quadtree algorithm was used to subsample the interferograms before modeling [e.g., *Jonsson et al.*, 2002]. Subsampling reduces the number of observation points to a computationally manageable number and mitigates the contribution of correlated errors between nearby pixels either inherent to the interferogram or introduced by filtering. The quadtree algorithm samples the interferograms more densely in high-variance areas. The result is that actively deforming areas have a greater weight in the model inversion (Figure 3).

2.2. Global Positioning System

[19] We use the coseismic Global Positioning System (GPS) displacements of *Rolandone et al.* [2006]. The set consists of 35 stations, including continuous stations in the SCIGN Parkfield Network, four continuous stations operated by the University of Wisconsin [*Titus et al.*, 2005] and campaign observations by the USGS, JPL, and UC Berkeley (Figure 1). For the continuous stations, the coseismic displacements are the difference between the average of 4 days before and the average of the 4 days after the San Simeon earthquake. For the campaign stations, the pre-earthquake position was extrapolated using an estimated interseismic velocity. The interseismic velocities were determined either by fitting a time

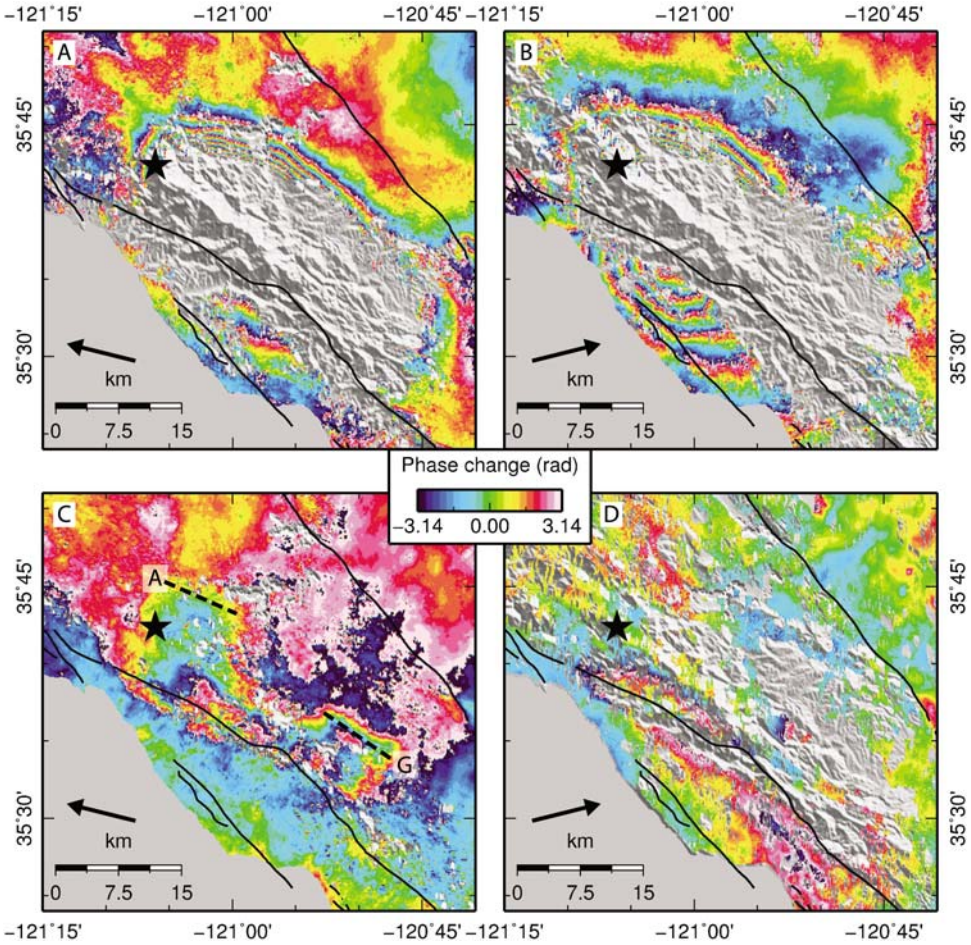

Figure 2. Wrapped interferograms spanning from (a) 9 July 2003 to 14 April 2004, (b) 9 December 2003 to 14 September 2004, (c) 31 December 2003 to 4 February 2004, and (d) 20 January 2004 to 1 April 2004 (see Table 1). Black star is SSEQ epicenter; black lines are mapped fault traces. Arrows show horizontal projection of the satellite look vector. Dashed lines labeled "A" and "G" are lineaments identified in interferogram C by *McLaren et al.* [2008].

series of preearthquake observations or from the SCEC Crustal Motion Map (http://epicenter.usc.edu/cmm3/). When available, the postearthquake positions for the campaign stations were also taken to be the average of the first 4 days after the earthquake. When postevent observations occurred more than 4 days after the San Simeon earthquake, *Rolandone et al.* [2006] corrected them for postseismic motions by using a model of afterslip derived from six postseismic time series to estimate the displacements between the time of the earthquake and the first observation (http://quake.wr.usgs.gov/research/deformation/gps/). The uncertainties in the GPS displacements from *Rolandone et al.* [2006] reflect both the formal errors from the position processing as well as the uncertainties in interseismic velocities or postseismic correction, when used.

3. Model Geometry

[20] Aftershocks from the San Simeon earthquake appear to outline not just the coseismic slip plane but also several subconjugate structures. *McLaren et al.* [2008] identified five structures from relocated aftershocks; the coseismic (main) rupture plane, one small plane subparallel to and to the south of the main rupture, and three west-dipping structures (back thrusts). One backthrust is to the northwest, near the earthquake hypocenter, and is clearly defined by aftershocks. The other two are to the southeast, within more diffuse seismicity. We use a subset of the planes identified by McLaren et al. as the starting model for a constrained nonlinear search for the best-fitting dislocations. We simplify the model geometry by excluding the small subparallel plane and combining the two backthrusts in the south into one structure. McLaren et al. presented interferogram C as evidence that these backthrusts accommodated shallow afterslip; it is less clear whether these planes also slipped coseismically. While our data contain a mixture of coseismic and postseismic deformation, we will attempt to separate them as well as possible and address this question.

[21] Data from all four interferograms and the coseismic GPS were used to determine a single set of dislocations for both the coseismic and postseismic periods. To account for the various time spans and therefore various slip distributions contained in each data set, the length, width, depth, and slip were allowed to vary for each set. The strike and surface

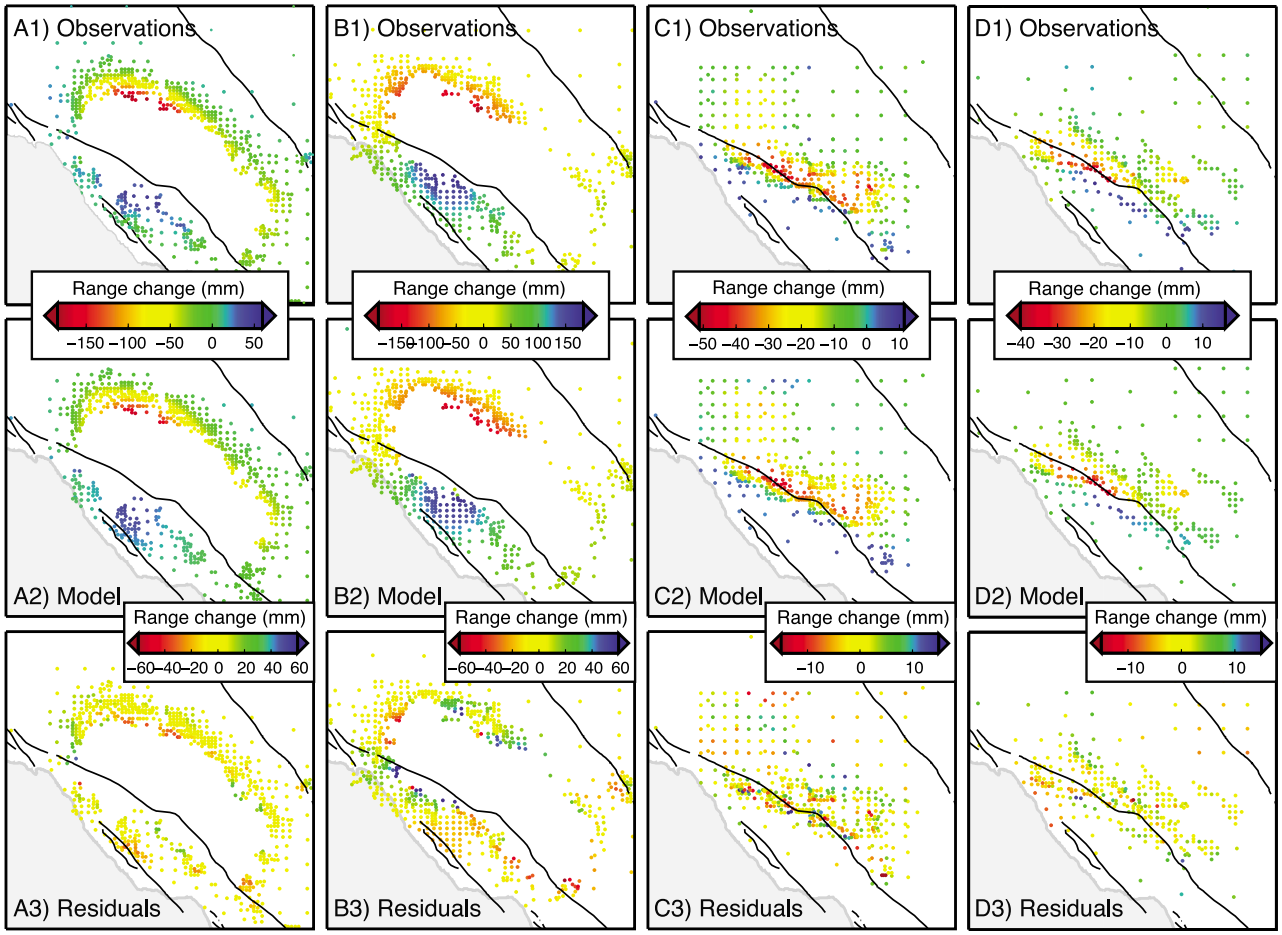

Figure 3. InSAR data and modeled samples used in the inversions, obtained using a quadtree algorithm. Modeled data are for our final model $C_{mb_s} P^{exp}_{mb_s} P_{mb_n}$ (see text). Subfigure letters as the same as those given in Table 1 and used in the text: (a) 9 July 2003 to 14 April 2004, (b) 9 December 2003 to 14 September 2004, (c) 31 December 2003 to 4 February 2004, and (d) 20 January 2004 to 1 April 2004.

projection of each structure was constrained to be the same across the data sets. Fault dip can be poorly constrained when using only surface data; we therefore fix our fault plane dips to those of *McLaren et al.* [2008]. For the merged southeast backthrust plane the dip was fixed to the average of the values of the two McLaren et al. planes. Variable rake angle was allowed but constrained to within ±45° of pure thrust using a bounded-value least squares algorithm [*Stark and Parker*, 1995]. The inversion was set up according to equation (1):

$$[\mathbf{G} \quad \mathbf{xy}]^{-1} \vec{\mathbf{d}} = \begin{bmatrix} \vec{\mathbf{s}} \\ \vec{\mathbf{t}} \end{bmatrix} \tag{1}$$

where $\vec{\mathbf{d}}$ is the vector of data values and $\mathbf{G}$ is the Green's function calculated using Okada's equations for displacements at the surface due to slip ($\vec{\mathbf{s}}$) on a buried dislocation in an elastic half-space [*Okada*, 1985]. Here $\mathbf{xy}$ is the matrix of Green's functions relating the interferogram samples to an offset and gradient across the interferogram ($\vec{\mathbf{t}}$); the elements in $\mathbf{xy}$ corresponding to the GPS data are zero. A gradient is generally included as a model parameter for inversions of InSAR data to compensate for possible errors in satellite orbit parameters [e.g., *Bürgmann et al.*, 2000].

[22] We seek to minimize the weighted-residual sum of squares (WRSS), given by

$$WRSS = \sum_n \gamma_n \left(d_n - \hat{d}_n \right)^2 \tag{2}$$

where d_n are elements of the data vector and $\hat{d}_n$ are the model predicted values. Here γ_n is the weighting factor for each interferogram and was chosen such that $|\gamma \vec{\mathbf{d}}|$ is equal for each data set.

[23] The final model geometry was arrived at iteratively; the planes were added into the search one at a time, with the output of the first search used as the starting geometry for that plane in the next. Additionally, the planes were first fit to the postseismic interferograms, where the backthrust structures are the most apparent; then the coseismic interferograms were added in to determine the final set of dislocations (see Table 2).

[24] Though we search for a best-fitting model geometry, it does not vary much from our starting model, that of *McLaren et al.* [2008]. There are two main differences. The first is that our data prefer a slightly more westerly strike for the northern backthrust than for the other two faults. Second, the InSAR

data place the southern backthrust ~3 km southwest of the two southern backthrusts of McLaren et al. Its placement is controled by a high deformation gradient in the postseismic interferograms, implying near-surface faulting. However, the subsurface projection does not intersect the southern cluster of aftershocks. The double-difference relocated aftershocks [*Hardebeck et al.*, 2004] are offset by about 3–3.5 km in the horizontal and 2–2.5 km in the vertical. Even when the dip constraints on this plane are loosened in the geometry search, the data do not prefer a steeper dip that might better line up with the aftershocks. This could be an indication that this backthrust has a listric, rather than planar, surface.

[25] The strike and position of the main rupture plane and the southern backthrust are well-constrained by interferogram C, which has sharp gradients that clearly indicate the near-surface edge of the planes. The positioning and orientation of the northern backthrust are less clearly defined, as there does not appear to be near-surface slip creating a visible delineation in the interferograms. While the aftershocks surrounding the northern backthrust may appear to match the more rotated trend of our geometry, this appearance is due to a deepening of the aftershocks toward the north. In fact, the trend of the plane defined by the aftershocks is oriented about 10° clockwise from our plane, more parallel to the main rupture. Some of the effects of a main plane parallel strike for the northern backthrust, as well as variations in the faults dips will be discussed in the following sections.

4. Distributed Slip Inversions

[26] In the previous section each interferogram and the GPS data were used to determine a set of planes that best fit each data set. No attempt was made to reconcile the fact that these data sets represent overlapping time spans and should be the result of consistent coseismic and postseismic slip histories. For the distributed slip inversions we not only subdivide the best-fitting fault geometries as determined above to obtain an estimate of the slip distributions, but we also invert the data sets jointly to determine a single coseismic and postseismic slip scenario.

[27] First, we assume a rupture scenario where the two back thrust planes are active only postseismically. Later, we add them to the coseismic slip model and evaluate whether this rupture scenario produces a substantially better fit to the data. We label the model realizations by indicating which structures are active in the coseismic (C) and postseismic (P) periods. The active structures are indicated by the subscripts *all*, *m*, b_n, b_s, for all three structures, the main plane, the northern backthrust, and the southern backthrust, respectively. If the postseismic slip is assumed to decay exponentially, exp is added as a superscript.

4.1. Exponentially Decaying Afterslip

[28] We begin by using the approach of *Johanson et al.* [2006] to separate coseismic and postseismic deformation by assuming a functional form for the postseismic slip. In this work the postseismic deformation is assumed to decay according to an inverse exponential function [*Johanson et al.*, 2006; *Savage et al.*, 2003]

$$d_{post} = A_{post}\left(1 - e^{-t/\tau}\right), \tag{3}$$

where t is the time since the earthquake, A_{post} is the total amount of postseismic slip as t goes to infinity, and τ is the decay time constant that controls how quickly d_{post} approaches A_{post}. The use of an exponential function is somewhat arbitrary. We assume no physical mechanism by which postseismic deformation should necessarily follow such a function, but merely seek to describe the form of the decay observed in postseismic GPS data. Other authors have used logarithmic functions to describe postseismic decay and found them to also fit well [e.g., *Savage et al.*, 2005]. However, functions of the form $\ln(1 + t)$ have the undesirable property that they approach infinity with increasing t. That is to say, afterslip never decays away completely. Nonetheless, an inverse exponential is not the only usable function to approach a finite limit with increasing t; $\frac{1}{t}\ln(1 + t)$ and Omori's law, t^{-n} where n is any positive number [*Savage et al.*, 2007], also have finite limits and can be used to satisfactorily fit curves observed in postseismic GPS data. We find that for post-San Simeon GPS data, there is little difference in the fit to the data of these alternate functions versus an inverse exponential and therefore continue to use equation (3).

[29] Here τ was estimated by curve fitting time series of GPS data from 10 stations processed by the USGS and located near the San Simeon earthquake rupture area. Four are campaign stations with daily observations for about the first month following the earthquake and subsequent observations in February, March, and July of 2004. These stations provide the only record of motion near the rupture area in the first 2 weeks. Five stations are Plate Boundary Observatory (PBO) stations installed quickly following the SSEQ, between 11 January 2004 and 1 February 2004. This set of stations produced values for τ ranging from 0.06 to 5.5 years and we use a central value of 0.1 years in our modeling (see auxiliary material Figure S1).[1]

4.2. Inversion Formulation

[30] The fault planes determined from the nonlinear search were subdivided into roughly 2 × 2 km elements. The inversions were carried out using a bounded-value least squares algorithm [*Stark and Parker*, 1995] to constrain the modeled rake angle to be within ±45° of pure thrust. The basic inverse formulation followed throughout this work is given by equation (4):

$$\begin{bmatrix} \mathbf{WG} \\ \beta\nabla^2 \end{bmatrix}^{-1} \begin{bmatrix} \mathbf{W}\vec{\mathbf{d}} \\ \mathbf{0} \end{bmatrix} = \vec{\mathbf{m}} \tag{4}$$

where **G** is the matrix of Green's functions relating unit slip on buried dislocations to deformation at the surface using Okada's equations [*Okada*, 1985]. **W** is the matrix of weights for each data set, $\vec{\mathbf{d}}$ is the vector of data values, and $\vec{\mathbf{m}}$ is the vector of model parameters. The formulation includes Laplacian smoothing (∇^2) with a weight (β) chosen by examining a tradeoff curve of misfit versus model roughness (Figure 4) for a joint inversion with the final rupture scenario and selecting a value that provides a smooth model with minimal increase in misfit.

[31] The smoothing weight for all other model geometries was chosen to match the ratio of smoothing to the Green's

[1] Auxiliary materials are available in the HTML. doi:10.1029/2009JB006599.

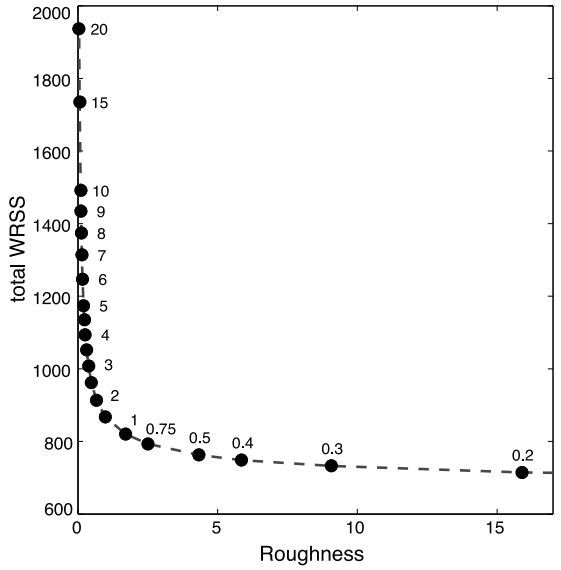

Figure 4. Tradeoff curve of weighted-residual sum of squares (WRSS) misfit versus model roughness for $C_{mb_s} P^{exp}_{mb_s} P_{mb_n}$. Roughness is calculated as $|\nabla^2 \vec{\mathbf{m}}|^2$, with symbols as in equation (4). Data labels are the corresponding values for the ratio $|\beta\nabla^2|/|\gamma \mathbf{G}_s + \mathbf{W}_g \mathbf{G}_g|$; 1.5 was chosen as the optimal value for this model. Here β for the other models was varied to keep this ratio constant across all inversions.

function kernel. That is, $|\beta\nabla^2|/|\gamma \mathbf{G}_s + \mathbf{W}_g \mathbf{G}_g|$, is kept constant for all geometries and held to the value (1.5) from the joint inversion on model $C_{mb_s} P^{exp}_{mb_s} P_{mb_n}$.

[32] In all cases, $\mathbf{W}$ and $\vec{\mathbf{d}}$ are as given in equation (5):

$$\mathbf{W} = diag \begin{bmatrix} \gamma_a \\ \gamma_b \\ \gamma_c \\ \gamma_d \\ \mathbf{W_{gps}} \end{bmatrix}, \quad \vec{\mathbf{d}} = \begin{bmatrix} \vec{\mathbf{d}}_a \\ \vec{\mathbf{d}}_b \\ \vec{\mathbf{d}}_c \\ \vec{\mathbf{d}}_d \\ \vec{\mathbf{d}}_{gps} \end{bmatrix}, \tag{5}$$

where the subscripts *a*, *b*, *c*, and *d* refer to interferograms A, B, C, and D from Table 1 and the subscript *gps* refers to the GPS data. The GPS data are weighted by the inverse covariance matrix (χ^{-1}) given by $\mathbf{W}^T_{gps}\mathbf{W}_{gps} = \chi^{-1}$. The InSAR data are assumed to be independent and have constant data variances within a data set. The parameters γ_n were chosen so that each InSAR data set is evenly weighted relative to each other and the GPS data. That is, $|\gamma_n \vec{\mathbf{d}}_n| = |\mathbf{W_{gps}} \vec{\mathbf{d}}_{gps}|$ for $n = a, b, c$, and d.

4.3. *F* test

[33] The *F* test compares two models, one of which is a subset of the other, and provides a confidence level $(1 - \alpha)$ for whether the improvement in misfit for the more complex model justifies the extra model parameters [e.g., *Stein and Gordon*, 1984]. Here it is used as guidance on whether more complicated coseismic or postseismic slip geometries are supported by the data. Here α is the area under the F distribution curve at F_{calc} where

$$F_{calc} = \frac{(WRSS_1 - WRSS_2)/(DOF_1 - DOF_2)}{WRSS_2/(DOF_2)} \tag{6}$$

DOF is the number of degrees of freedom in the model, given by $N_{data} - N_m$, where N_{data} is the number of data points and N_m is the number of model elements. The F distribution curve used to determine α is constructed using the number of degrees of freedom for the numerator and denominator of equation (6), which in this case is $DOF_1 - DOF_2$ and DOF_2, respectively.

[34] There are several factors in our model inversions which cause the *F* test to be an imperfect measure of whether added complexity is justified. First, we include two constraints (positivity and smoothing) on our model which result in the model parameters not being independent, an underlying assumption of the *F* test. The effect of the positivity constraint is mitigated by removing the model elements with values at the bound (inactive elements) from the calculation of DOF, such that $DOF = N_{data} - (N_m - N_{inactive})$. This is identical to removing the inactive elements from the model inversions and can have the effect of changing the models so that the simple model is no longer a subset of the complex model. Also, the large number of data points used here relative to model parameters produce a narrow spread in the WRSS values that result in significance levels of 5% and 95%. The *F* test results then tend to fluctuate between 0% and 100% significance and provide little information for comparing between *F* test results.

[35] Despite these problems, the *F* test can still provide guidance on whether more complex models are justified. It at least provides some context for how much of an improvement a given decrease in WRSS represents, though we do not follow its results strictly here.

4.4. Uniformly Decaying Afterslip

[36] The data are first inverted under a simple scenario involving coseismic slip on the main plane (*m* in Table 2) and uniformly decaying afterslip in the postseismic period. Here the matrix $\mathbf{G}$ is a container for all the Green's functions for

Table 1. Interferograms Used in This Study[a]

Interferogram Letter	Scene ID	Start Date (t_1)	End Date (t_2)	⊥ Baseline (m)	Look Angle
A	ERS D 27/2889	9 Jul 2003	14 Apr 2004	46	23°
B	Envisat A 206/711	9 Dec 2003	14 Sep 2004	71	23°
C	ERS D 27/2889	31 Dec 2003	4 Feb 2004	−212	23°
D	Radarsat A 42854-43883	20 Jan 2004	1 Apr 2004	3	29°

[a]Interferograms are identified in the text by the letter in the first column. In the Scene ID column, ERS and Envisat scenes are identified by track/frame numbers and RSAT scenes are identified by start-end orbit numbers; A and D refer to ascending or descending orbit track, respectively.

Table 2. Final Estimated Fault Geometry Parameters[a]

Fault Plane	Strike	Dip	Length (km)	Width (km)	Top, Center Point	
					Latitude	Longitude
m	295°	45°	40	18	35.582	−121.006
b_n	109°	60°	15	20	35.755	−121.074
b_s	116°	32°	20	14	35.635	−120.865

[a]All planes project to the surface, i.e., top, and center point is at zero depth. Here m refers to the main rupture plane, b_n refers to the northern backthrust, and b_s refers to the southern backthrust.

each data set and fault model as given by Okada's equations and described in section 3

$$\mathbf{G} = \begin{bmatrix} \mathbf{G}_{Ca} & \left(1 - e^{-t_{a2}/\tau}\right)\mathbf{G}_{Pa} & \mathbf{xy}_a \\ \mathbf{G}_{Cb} & \left(1 - e^{-t_{b2}/\tau}\right)\mathbf{G}_{Pb} & \mathbf{xy}_b \\ \mathbf{0} & \left(e^{-t_{c1}/\tau} - e^{-t_{c2}/\tau}\right)\mathbf{G}_{Pc} & \mathbf{xy}_c \\ \mathbf{0} & \left(e^{-t_{d1}/\tau} - e^{-t_{d2}/\tau}\right)\mathbf{G}_{Pd} & \mathbf{xy}_d \\ \mathbf{G}_{Cgps} & \mathbf{0} & \mathbf{0} \end{bmatrix} \quad (7)$$

[37] The postseismic Green's functions are scaled according to the portion of the postseismic time interval the interferogram covers, from their beginning date (t_1) to their end date (t_2). For interferograms spanning the coseismic period, their scaling depends only on the end dates (t_2, see Table 1) and the decay constant (τ). The model vector (equation (8)) contains the amplitude of the postseismic decay function (A_{post} in equation (3)), which is the total postseismic slip,

$$\vec{\mathbf{m}} = \begin{bmatrix} \vec{\mathbf{s}}_C \\ \vec{\mathbf{A}}_P \\ \vec{\mathbf{t}} \end{bmatrix} \quad (8)$$

[38] We find that including exponential decay on the main plane and either the northern or southern backthrust ($C_mP^{exp}_{mb_n}$ or $C_mP^{exp}_{mb_s}$) fits the data better than decaying afterslip on only the main rupture plane ($C_mP^{exp}_m$) at the 98% and 100% significance level, respectively. Including decaying afterslip on all three planes ($C_mP^{exp}_{all}$) improves the fit to the data at the 100% significance level over model $C_mP^{exp}_{mb_n}$, implying that the southern backthrust is necessary regardless of whether the northern backthrust is also included. However, model $C_mP^{exp}_{all}$ does not provide a significant improvement in fit to the data (0%) over model $C_mP^{exp}_{mb_s}$, suggesting that the addition of the northern backthrust is unjustified and the data are well fit by decaying afterslip on the main plane and southern backthrust.

Table 4. Summary of Variance Reductions of Data Sets to Distributed Slip Models[a]

Model	Interferograms				GPS
	A	B	C	D	
$C_mP^{exp}_{all}$	90.1%	82.7%	73.7%	88.0%	87.9%
$C_mP^{exp}_{mbs}$	89.5%	83.4%	71.5%	87.4%	87.8%
$C_mP^{exp}_{mbs}P_m$	89.4%	82.9%	85.9%	87.8%	87.7%
$C_mP^{exp}_{mbs}P_{bn}$	90.6%	83.5%	74.5%	87.6%	88.1%
$C_mP^{exp}_{mbs}P_{bs}$	90.2%	83.8%	74.6%	87.7%	87.9%
$C_mP^{exp}_{mbs}P_{mbn}$	90.4%	83.3%	84.7%	87.9%	88.0%
$C_{mbs}P^{exp}_{mbs}P_{mbn}$	92.0%	90.8%	85.1%	87.9%	88.7%

[a]Model naming convention is described in Table 3 and specific model descriptions are in the text.

[39] The variance reductions of the individual data sets (Table 4) show how well each is fit by the models. Model $C_mP^{exp}_{mb_s}$ provides the best fit to interferogram A (89.5%), while the GPS data and D are the next well fit at 87.4% and 87.8%, respectively. Interferogram B is less well fit, with a variance reduction of 83.4% and C is particularly poorly fit, with a variance reduction of only 71.5%. The likely reason for the large difference in fit to C versus D (also only postseismic) is that C includes a lobe of range decrease northeast of the SSEQ epicenter that is not present in D and has a lobe of deformation centered on the main rupture plane that is extended further south than in D. When this occurs for two interferograms with different look directions (C is descending mode and D is ascending), it can be an indication that deformation occurred only horizontally, in a direction to which one interferogram is insensitive (in this case, perpendicular to the horizontal look direction of D). However, there is no obvious mechanism for causing only horizontal motion. Thrust faulting, fault opening, and even strike-slip faulting all cause some amount of vertical motion, which should be detectable in D. Another scenario, which we favor, is that deformation in the northeast was completed before the time spanned by interferogram D.

4.5. Extra Postseismic Slip

[40] To help fit interferogram C better, we consider a slip scenario with extra slip during the timespan of interferogram

Table 3. F Test Results for Coseismic and Postseismic Model Inversions of Varying Complexity[a]

Model 1	WRSS 1	Model 2	WRSS 2	$1-\alpha$	Improvement in WRSS (%)	5%–95% Spread
$C_mP^{exp}_m$	1249	$C_mP^{exp}_{all}$	1089	100%	15.7%	4.7%–7.0%
$C_mP^{exp}_{mbs}$	1116	$C_mP^{exp}_{all}$	1089	0%	2.4%	2.9%–4.8%
$C_mP^{exp}_{mbn}$	1202	$C_mP^{exp}_{all}$	1089	100%	9.4%	2.4%–4.2%
$C_mP^{exp}_{mbs}$	1116	$C_mP^{exp}_{mbs}P_m$	1063	0%	4.7%	8.0%–10.9%
$C_mP^{exp}_{mbs}$	1116	$C_mP^{exp}_{mbs}P_{bn}$	1077	19%	3.5%	3.0%–5.1%
$C_mP^{exp}_{mbs}P_m$	1063	$C_mP^{exp}_{mbs}P_{mbn}$	1042	88%	2.0%	0.9%–2.2%
$C_mP^{exp}_{mbs}P_{mbn}$	1042	$C_{mbn}P^{exp}_{mbs}P_{mbn}$	1024	0%	1.7%	3.5%–5.6%
$C_mP^{exp}_{mbs}P_{mbn}$	1042	$C_{mbs}P^{exp}_{mbs}P_{mbn}$	871	100%	16.4%	1.7%–3.5%

[a]Uppercase C refers to coseismic model planes and uppercase P refers to postseismic. Subscripts refer to which structures are active during the indicated time (C or P); m = main rupture plane, b_n = northern backthrust, b_s = southern backthrust. Superscript exp indicates postseismic structures included in uniform decay; no superscript indicates structures included in extra slip during the time span of interferogram C. See text for specific model descriptions. Weighted-residual sum of squares (WRSS) is calculated according to equation (2). Here $1-\alpha$ is the significance level of improvement in WRSS for the more complex model. The 5%–95% spread shows the percent improvements in WRSS which would have resulted in 5% and 95% significance for the given two models being compared.

C in addition to the uniform decaying afterslip. This modifies the matrix of Green's functions and the model vector,

$$\mathbf{G} = \begin{bmatrix} \mathbf{G}_{Ca} & \left(1 - e^{-t_{a2}/\tau}\right)\mathbf{G}_{P1a} & \mathbf{G}_{P2a} & \mathbf{xy}_a \\ \mathbf{G}_{Cb} & \left(1 - e^{-t_{b2}/\tau}\right)\mathbf{G}_{P1b} & \mathbf{G}_{P2b} & \mathbf{xy}_b \\ \mathbf{0} & \left(e^{-t_{c1}/\tau} - e^{-t_{c2}/\tau}\right)\mathbf{G}_{P1c} & \mathbf{G}_{P2c} & \mathbf{xy}_c \\ \mathbf{0} & \left(e^{-t_{d1}/\tau} - e^{-t_{d2}/\tau}\right)\mathbf{G}_{P1d} & \mathbf{0} & \mathbf{xy}_d \\ \mathbf{G}_{Cgps} & \mathbf{0} & \mathbf{0} & \mathbf{0} \end{bmatrix} \quad (9)$$

$$\vec{\mathbf{m}} = \begin{bmatrix} \vec{\mathbf{s}}_C \\ \vec{\mathbf{A}}_{P1} \\ \vec{\mathbf{s}}_{P2} \\ \vec{\mathbf{t}} \end{bmatrix} \quad (10)$$

[41] Notations in equations (9) and (10) are identical to those in equations (7) and (8). Note that the extra slip is also included for interferograms A and B, which both also span the time period of interferogram C. Extra postseismic slip on the main rupture, southern backthrust or northern backthrust (individually) improves the fit to the data at the 0%, 48%, and 19% significance levels, respectively. However, despite having a significance level of 0% from the F test for the improvement for the model with extra slip on the main rupture plane ($C_m P^{exp}_{mb_s} P_m$), this model produces the largest improvement in variance reduction for interferogram C (Table 4). It improves from 71.5% to 85.9% for $C_m P^{exp}_{mb_s} P_m$, as compared to 74.5% for extra slip on only the northern back thrust ($C_m P^{exp}_{mb_s} P_{b_n}$) and 74.6% for extra slip on only the southern backthrust ($C_m P^{exp}_{mb_s} P_{b_n}$). The extra slip was specifically added because of the poor fit of model $C_m P^{exp}_{mb_s}$ to interferogram C and $C_m P^{exp}_{mb_s} P_m$ does a better job of fitting C than the other two models, we therefore use this as a basis to include extra slip on the main rupture plane despite its poor showing in the F test.

[42] For extra slip on both the main plane and the northern backthrust ($C_m P^{exp}_{mb_s} P_{mb_n}$) the significance level for the improvement over $C_m P^{exp}_{mb_s} P_m$ is 88%. This is mostly due to small increases in the variance reductions for interferograms A and B, while interferogram C is less well-fit with the northern backthrust than without. However, the northern backthrust is clearly defined by aftershocks and is near a lineament (A in Figure 2c) identified by *McLaren et al.* [2008] as indicating fault motion. While copious aftershocks do not necessarily mean that aseismic slip occurred, these reasons combined with the results of the F test, lead us to choose a model that allows some slip on the northern back thrust.

4.6. Coseismic Slip on Conjugate Planes

[43] We also investigate whether slip on the backthrust planes is indicated in the coseismic model. The northern and southern backthrusts were individually added to the coseismic fault geometry and tested against a model with coseismic slip only on the main plane. All tested models had the postseismic fault geometry settled on above ($C_m P^{exp}_{mb_s} P_{mb_n}$). Adding the northern backthrust to the coseismic fault geometry ($C_{mb_n} P^{exp}_{mb_s} P_{mb_n}$) improves the WRSS by 1.7% and the F test returns a significance level of 0%. However adding the southern backthrust ($C_{mb_s} P^{exp}_{mb_s} P_{mb_n}$) decreases the WRSS by 16.4%, an improvement at the 100% significance level. The improvement is substantial enough for us to choose the model with coseismic slip on the southern backthrust as our preferred model (Figure 5).

4.7. Discussion of Slip Models

4.7.1. Coseismic Slip

[44] Separating coseismic from postseismic slip using geodetic data, especially InSAR, is a difficult problem. In cases of rapid afterslip, it is likely that coseismic slip models will include some amount of aseismic slip. The GPS is the only data set we use that attempts to capture only coseismic motion, and in this case it includes campaign data with post-earthquake observations 1–2 days after the event. It is likely, then, that our "coseismic" model contains at least a couple days worth of postseismic slip.

[45] Including coseismic slip on the southern backthrust improved the fit of the model to the data at the 100% confidence level. The improvement is mostly due to the better fit of interferogram B, which has the longest timespan of all the interferograms, from before the earthquake on 9 December 2003 to 14 September 2004. It is possible then that the back thrust slip attributed to the coseismic model actually occurred during this later time period. However, if this were the case, one would expect the other coseismic data sets to have a worse data fit. Instead they are slightly improved, supporting the interpretation that the backthrust slip occurred either during the earthquake or soon after. Though it shows the smallest improvement in variance reduction, the improved fit to the azimuths of the GPS data demonstrate where the back thrust provides improved fit in all the data (Figure 6).

[46] The amount of moment release in our model compares favorably with others'. In our model nearly one third of the coseismic moment release occurs on the southern backthrust ($2.4 \times 10^{18} Nm$), with the main plane releasing 5.9×10^{18} Nm. The results on the main plane is similar to that found by *Ji et al.* [2004] (6.2×10^{18} Nm) using strong motion and teleseismic waveforms, together with 1-hz GPS data. It is also similar to the moment release reported by *Hardebeck et al.* [2004] of (5.7×10^{18} Nm) from only seismic data. Our total coseismic moment (8.3×10^{18} Nm) is more similar to that determined by *Rolandone et al.* [2006] ($7.85 \times 10^{18} Nm$), who use the same GPS data used here as well as strong motion seismic data to constrain a coseismic slip model. It would appear that the better the coseismic period is constrained (by using high-rate data), the lower the estimated moment release and these amounts are consistent with coseismic slip on only the main plane. The slip pattern on the main rupture plane is also similar to that found by other authors, in that it is elongated along-strike with peak slip of 1.9 m and near 8 km depth (Figure 5a). However, the peak slip is much closer to the hypocenter than is found in the model of *Ji et al.* [2004] and the rupture is more compact (though this would be affected by smoothing).

[47] Though most of the coseismic slip occurs at midlevel depths (6–10 km), the model predicts as much as 1 m of coseismic surface slip. This amount of surface slip is refuted by field surveys conducted immediately following the earthquake, which found no evidence of surface faulting [*Hardebeck et al.*, 2004]. The roughly 2 × 2 km element size may account for the high surface slip prediction when large slip deeper in the element dominates its slip result. Another possibility is that because the coseismic interferograms have a gap in coverage over the Coast Ranges, the sparse data allow the

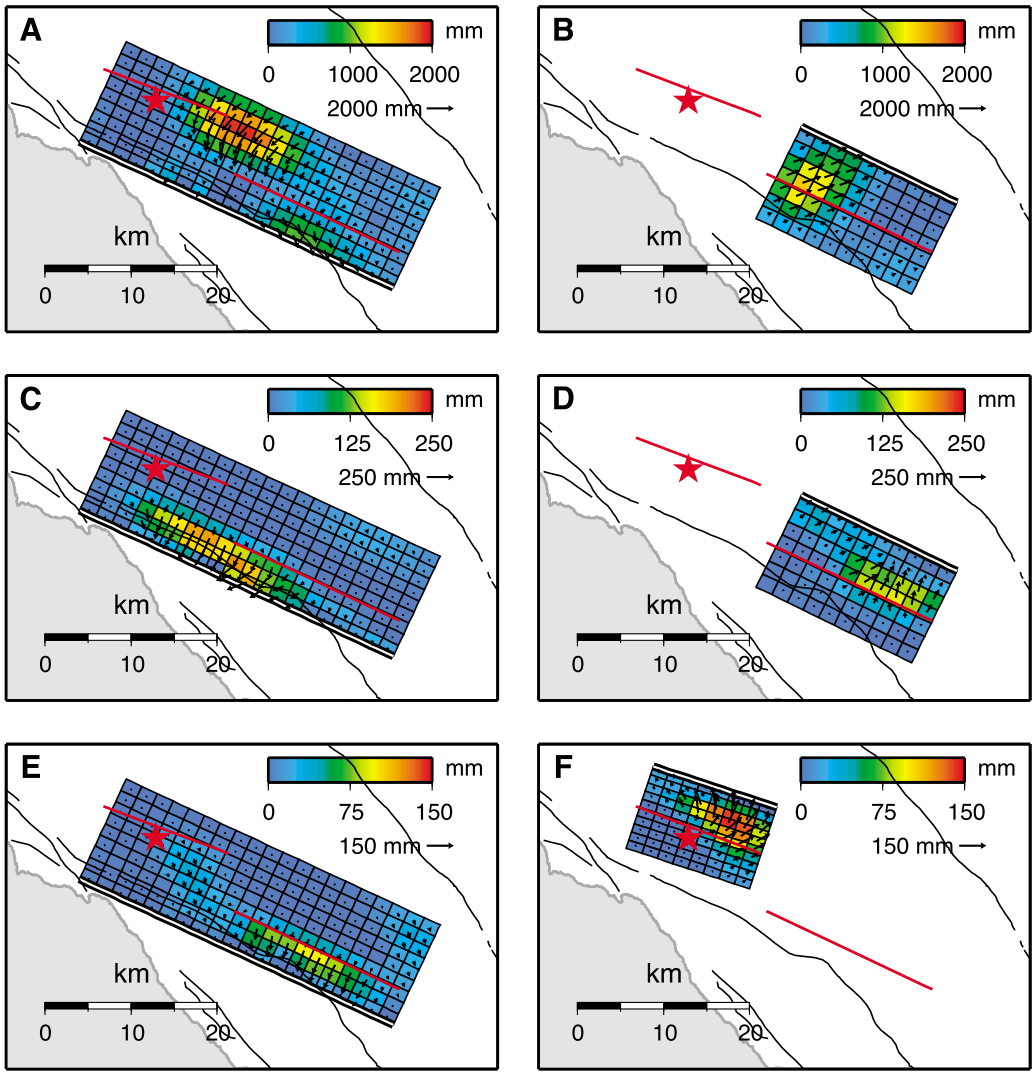

Figure 5. Distributed slip models from an inversion following equations (4) and (9) and allowing a rake angle within 45° of pure dip slip. Arrows represent movement of hanging wall block relative to footwall. Double line indicates top edge of model plane. (a and b) Coseismic slip on main plane and southern backthrust. (c and d) Postseismic slip subject to exponential decay on the main plane and the southern backthrust. (e and f) Extra slip early in the postseismic period on the main plane and the northern backthrust. Red star is the San Simeon earthquake epicenter. Red lines mark the location in map view of the lines of intersection between the main and backthrust planes.

Laplacian smoothing to smear deeper slip into the shallow elements.

4.7.2. Postseismic Slip

[48] Shallow afterslip can occur rapidly and produce nearly as much slip as the coseismic rupture. The Northridge and Loma Prieta earthquakes, both thrust mechanism events in California, included postseismic moment releases of 22% and 7%, respectively, of the coseismic [*Donnellan and Lyzenga*, 1998; *Segall et al.*, 2000]. The 2004 Parkfield earthquake was followed by shallow postseismic slip of magnitude in excess of the coseismic [*Langbein et al.*, 2006; *Johanson et al.*, 2006], largely attributed to the large amount of velocity-strengthening material in the fault as evidenced by interseismic creep. Here our model estimates $8.3 \times 10^{18} Nm$ (M_w6.5) of coseismic moment and 1.16×10^{18} (M_w6.0) of total postseismic moment (using a rigidity of 30 GPa). This means the postseismic period had a moment release of at least 14% of the coseismic. In actuality, this percentage is probably higher, since the coseismic model likely contains some postseismic slip. Nonetheless, this much postseismic slip is consistent with other thrust earthquakes in California and with the Oceanic fault being otherwise noncreeping.

[49] Though small compared to the coseismic slip, the postseismic slip distribution is not simple. The change in the location of shallow slip on the main rupture plane between the "extra slip" and exponential decay portions of the model may be an indication that slip did not decay uniformly but decayed more quickly to the southeast. The continuous GPS data do not help confirm whether this was the case because of the gap between the earthquake and the installation of the

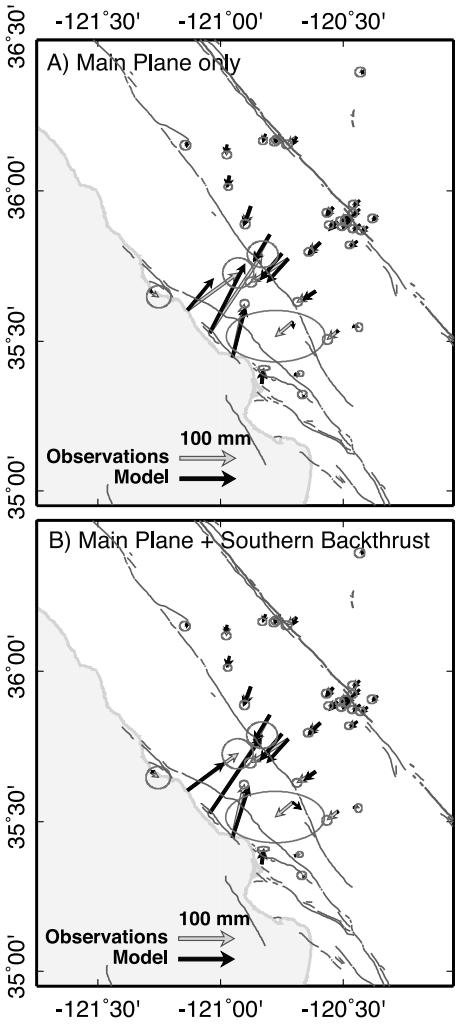

Figure 6. Comparison of the GPS data (grey vectors) and model predictions (black vectors) for model inversions (a) with ($C_m P^{exp}_{mb_s} P_{mb_n}$) and (b) without ($C_{mb_s} P^{exp}_{mb_s} P_{mb_n}$) coseismic slip on the southern backthrust structure. Data shown with 95% confidence ellipses.

PBO stations. Of the four campaign stations, "2068" is closest to the southern portion of the main rupture plane and "2076" is closest to the northern portion. However, these two stations show similar motions in the first month following the earthquake and if anything, the more northern "2076" appears to decay faster. Nonetheless station "2068" is 7.5 km from the Oceanic fault, far away enough to be sensitive to more than just the southern portion of the fault.

[50] Shallow afterslip on the northern backthrust is tenuously allowed by our model. Although the *F* test returns an 88% significance level to the improvement in WRSS, the improvement is only by 2.0%. We included this fault plane because of the vigorous aftershock activity and the interpretation by *McLaren et al.* [2008] of a lineament near the northern backthrust in interferogram C that could be the result of fault slip. Including slip on this plane does not improve the fit to C, however, but does improve the fit to A and B. Both A and B span the coseismic period, but including the northern backthrust in the coseismic model ($C_{mb_n} P^{exp}_{mb_s} P_{mb_n}$) does not fit the data significantly better than not including it, possibly because the GPS data do not allow much slip on this plane. If the northern backthrust is not included at all in the model inversion ($C_{mb_s} P^{exp}_{mb_s} P_m$), the slip on the other planes remains similar to results shown in Figure 5, with the main difference that a slip patch appears near the SSEQ hypocenter in the "extra slip" time period on the main rupture plane (Figure S2).

[51] Postseismic slip on both the northern and southern backthrusts, as well as the main plane, tends to occur updip of the intersections between planes (red lines in Figure 5). This is consistent with a structural model of the San Simeon back thrusts that has them terminating at the main plane such that the deep elements for the backthrusts do not actually exist. Only the modeled coseismic slip on the southern backthrust extends much past the planes' intersection, though on the main rupture plane, there is no structural reason why afterslip could not occur below the backthrust intersection.

[52] Because of the scarcity of GPS data in the early postseismic period and because of the sparse time sampling of InSAR data, the time history of early afterslip is not well determined. We have not attempted to assign a time function to the "extra slip" portion of our model but instead to determine how much total slip occurred. By whatever mechanism, the extra slip would need to be finished by 20 January 2004, the start date of interferogram D. The slip could have occurred as a decay function with a faster decay time constant or as a discrete slip event. In either case, we may still be missing slip that occurred before the beginning of C. However, given the small amount of slip resolved for the "extra slip" and the fairly good variance reductions for each data set using our final model, we expect that the amount of missing slip is small.

4.7.3. Variations in Model Geometry

[53] During the fault geometry estimation, the dip of each fault plane was held fixed to that determined by *McLaren et al.* [2008]. We performed several inversions varying the dips of each structure to investigate how this might affect our results. Modifying the dips of the northern and southern back thrusts by ±15° does not lead to improvements in the data fit of more than 1%. Adjusting any of the planes to be steeper provides a poorer fit to all the data. Gentler dips on the back thrust structures lead to small improvements in WRSS (<1%) and similar slip patterns; however, a gentler dip (30°) on the main rupture plane resulted in a WRSS of 811, a 7% improvement. Nonetheless, this model resolves a large area of as much as 1.5 meters of coseismic surface slip, the peak slip in this model. Ultimately, the coseismic slip pattern that is not similar to that found by previous authors [*Ji et al.*, 2004; *Rolandone et al.*, 2006] and contradicts the lack of observed surface faulting [*Hardebeck et al.*, 2004] by a wide margin.

[54] The surface projection of the northern backthrust is not as clearly delineated in the interferograms as are the main plane and southern backthrust. Also, the aftershocks in this area define a plane that has a parallel strike to the main rupture. In an inversion with a northern backthrust plane that strikes parallel to the main rupture, the overall data fit and the variance reductions of the individual data sets are almost identical (0.1% WRSS difference). The slip on the northern backthrust is reduced and additional "extra slip" is added near the SSEQ hypocenter. The effect is halfway between the model of Figure 5 ($C_{mb_s} P^{exp}_{mb_s} P_{mb_n}$) and one with no northern

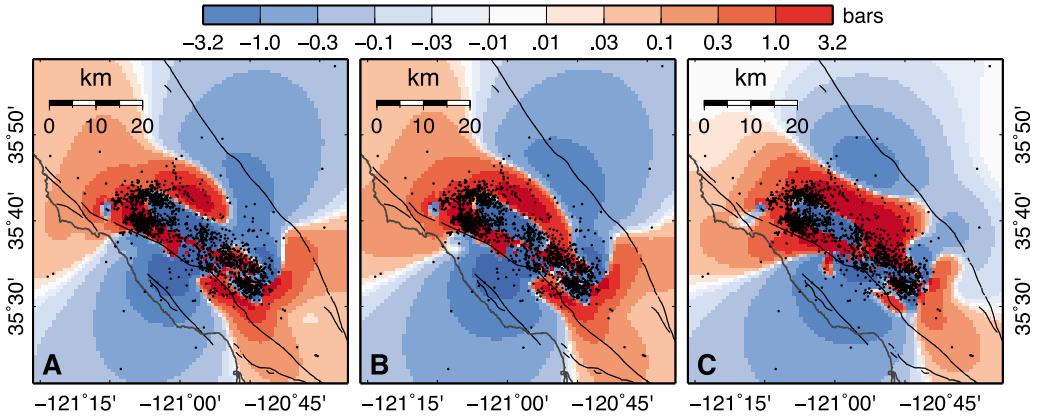

Figure 7. ΔCFS for planes in the orientations of the three structures used in this study; using μ' of 0.4 and calculated at a depth of 5 km. Black dots are relocated aftershocks from *Hardebeck et al.* [2004] with M ≥ 2. (a) For planes oriented parallel to the main rupture plane (strike = 295°, dip = 45°, rake = 90°); (b) parallel to the southern backthrust (strike = 116°, dip = 32°, rake = 90°); (c) parallel to the northern backthrust (strike = 109°, dip = 60°, rake = 90°).

backthrust ($C_{mb_s} P^{exp}_{mb_s} P_m$, Figure S2), indicating that there is a tradeoff between slip on the backthrust structure and deeper afterslip on the main rupture plane.

5. Static Stress Changes: Results and Discussion

[55] We calculate the static stress changes in the surrounding crust from our final model discussed above using the program Poly3D [*Thomas*, 1993] with a Poisson's ratio of 0.25 and shear modulus of 30 GPa. The change in Coulomb Failure Stress (ΔCFS) is commonly used to identify areas where slip in future earthquakes is promoted or inhibited [*Harris*, 1998; *Stein*, 1999]. ΔCFS is defined as

$$\Delta CFS = \Delta\tau + \mu'\Delta\sigma \tag{11}$$

ΔCFS is defined for a plane with a specific orientation and slip vector, termed the receiver fault. Accordingly, $\Delta\tau$ is the change in shear stress and $\Delta\sigma$ is the change in normal stress on that specific plane. The parameter μ is the coefficient of friction and can have values from 0 to 1. From laboratory experiments, μ has been found to be consistently 0.6–0.8 among many different rock types [*Byerlee*, 1978]. Pore fluid pressure within the fault can counteract $\Delta\sigma$; however, this effect can be neglected if μ is rescaled to become the effective coefficient of friction (μ') [*Harris*, 1998]. The abundance of fault gouge on more well-developed faults encourages the existence of high pore fluid pressures and μ' has been observed to depend on a fault's slip rate [*Parsons and Dreger*, 2000; *Parsons et al.*, 1999]. Earthquake triggering on established faults, such as the San Andreas, is then likely to depend more on shear stress changes, (where 0.4 is a commonly used value [e.g., *Stein et al.*, 1994; *Toda and Stein*, 2002]), whereas triggering on low-slip faults may depend more on normal stress changes [*Parsons et al.*, 1999].

5.1. Relationship to San Simeon Aftershocks

[56] The existence of several structures with different orientations, all producing aftershocks, makes it difficult to determine the optimal value of μ' quantitatively. In the northern part of the aftershock zone, two clusters are visible in map view, presumably corresponding to events on the main and northern backthrust. To the south, however, the aftershocks are not so easily separable. Even for aftershocks with available focal mechanisms, the near-orthongonal arrangement of the main and backthrust planes makes it difficult to definitively determine which nodal plane the aftershocks occurred on. We do our best to examine stress changes and relate them to aftershocks that occurred on the various structures but admit that our knowledge of the slip mechanisms of the aftershocks is incomplete at best.

[57] Because they are nearly orthogonal, the main plane and the two backthrusts have similar patterns of CFS changes (Figure 7); orthogonal planes have identical calculated shear stress changes but different normal stress changes. In the orientations of all three planes, the backthrust region experienced CFS increase of over 1 bar from coseismic slip, using $\mu' = 0.4$. This can be compared to a threshold of 0.1 bars for aftershock triggering established empirically from other events [e.g., *Harris*, 1998], providing some explanation for why the backthrust structures were activated. The areas of high ΔCFS in the backthrust region are areas of both increased shear stress and unclamping and would be a zone where aftershocks are encouraged regardless of the value of μ'. However, the area of maximum CFS change does not produce the most aftershocks, even though stress changes are well above 0.1 bars. Instead they occur in clusters that define the two backthrusts; possibly because these are preexisting structures that slip more readily than the surrounding intact region.

5.2. Stress Change and Afterslip on Backthrusts

[58] While there is uncertainty about the slip directions of the aftershocks, we have modeled afterslip that is presumably also driven by stress changes from the SSEQ. We calculate stresses resolved on the backthrusts by coseismic slip from the SSEQ and compare them to the patterns of afterslip.

[59] The Oceanic fault has characteristics that are consistent with both low and high μ'. Seismic wave speeds measured from aftershocks indicate high levels of crustal fluids in the San Simeon area [*Hauksson et al.*, 2004], which would

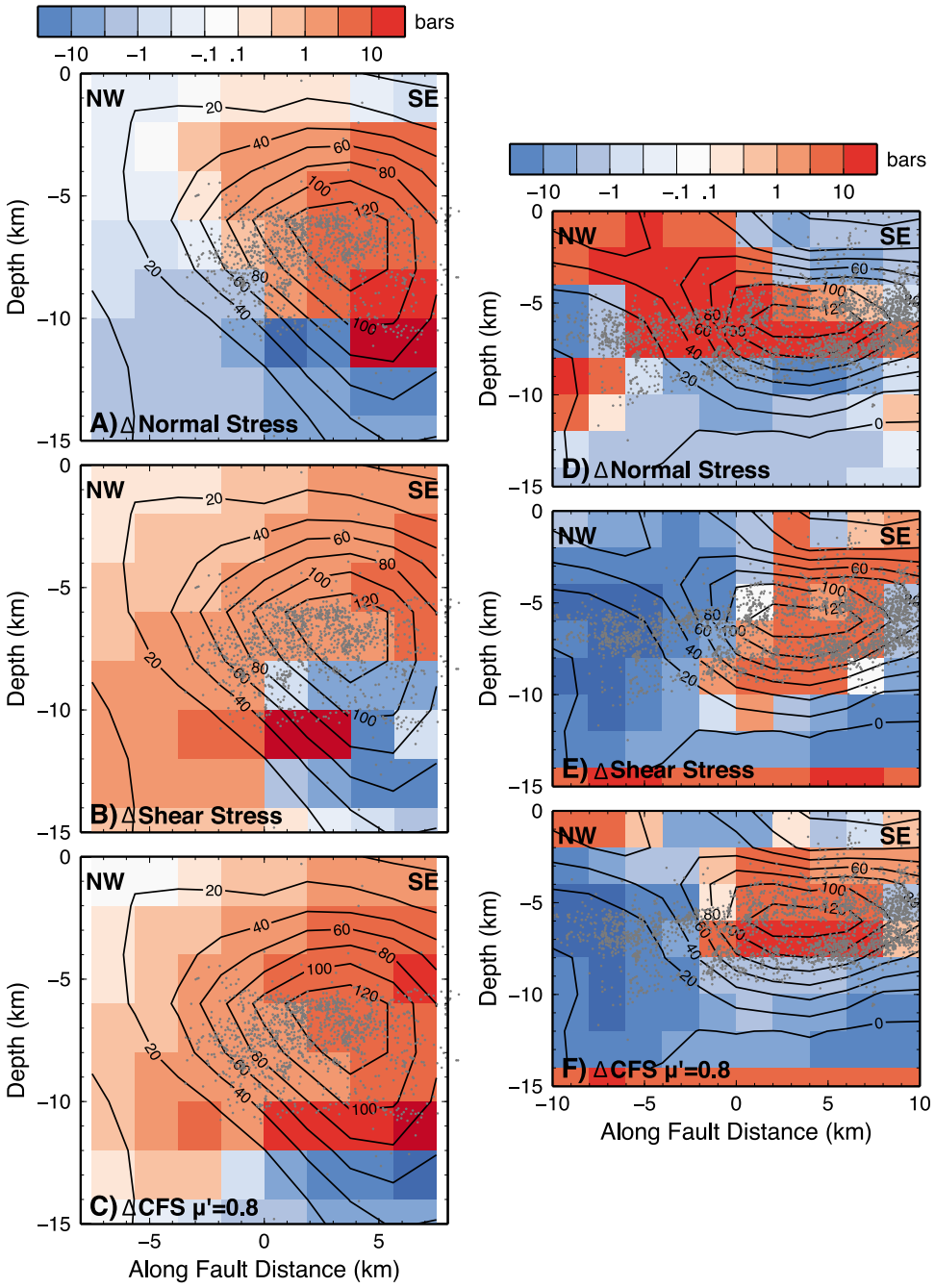

Figure 8. Stress changes (colors) due to coseismic slip and postseismic slip (contours in mm) for (a, b, c) the northern and (d, e, f) southern backthrusts. Shown with relocated aftershocks from *Hardebeck et al.* [2004] (grey dots). Figures 8a and 8d show normal stress changes, Figures 8b and 8e show shear stress changes, and Figures 8c and 8f show change in CFS using $\mu' = 0.8$. All stresses are calculated for pure thrust on the receiver fault. Gridding for the stress change calculation is identical to slip model grid spacing.

imply earthquake triggering should correlate more with changes in shear stress than normal (low μ'). However, the Oceanic fault is a low-slip fault, located in a thrust belt with similar tectonic setting as the Foothills thrust belt in the southern Bay Area. *Parsons et al.* [1999] found that earthquake triggering on the Foothills thrust belt following the 1989 Loma Prieta earthquake depended more on normal stress changes than shear (high μ').

[60] On the northern backthrust, the slipped area is consistent with both unclamping and increased shear stress in the thrust direction, though the shape of the slipped area corresponds better with the pattern of unclamping (Figure 8). Likewise on the southern backthrust, the afterslip area corresponds to both increased shear and unclamping stresses, but the pattern of unclamping matches the pattern of slip better than the shear stress changes (Figure 8). The area of peak

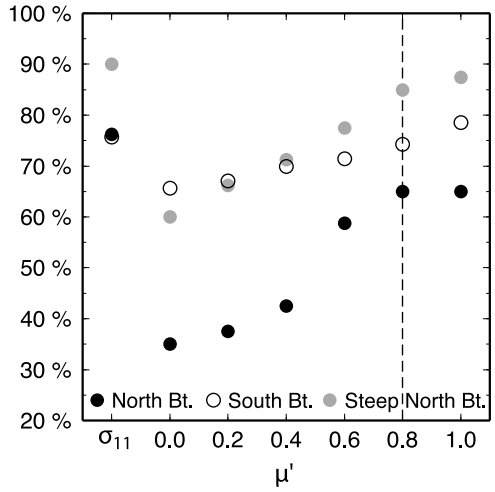

Figure 9. Percentage of elements in the slip models for aseismic slip on the northern and southern backthrusts that are consistent with CFS triggering for a given value of μ'. Also shown are the percentages for a plane similar to the northern backthrust, but with a steeper dip (75° rather than 60°). σ_{11} in the x-axis indicates the percentage corresponding to unclamping only. The dashed line is drawn for a value of $\mu' = 0.8$, where the values begin to approach those for unclamping only.

afterslip illustrates this: shear stress is clearly increased in this area but over a larger depth range than the afterslip, which tapers off above 5 km down-dip extent. The normal stress pattern shows unclamping in the same location as the slip but also shows clamping above 4 km.

[61] We define a simple measure of stress triggering to help determine μ' for afterslip triggering. We assume that model elements that experienced afterslip should correspond to increased CFS and elements with no afterslip should correspond to decreased ΔCFS. Because the curvature-minimizing Laplacian smoothing used in our inversions tends to spread small values of slip throughout the model fault plane, we choose a slip threshold of 20 mm, below which model elements are treated as having zero slip. The 20 mm threshold is equivalent to the second-to-outermost contour in Figure 8.

[62] For the northern backthrust, we find that 65% of the model elements are consistent with a stress triggering hypothesis with $\mu' = 0.8$. If only the normal stresses are considered, the percentage increases to 75% (Figure 9). The percent of consistent elements continues to increase for values of μ' greater than one, which are unphysical, and plateaus at a μ' of about 2.0, which yields 76%.

[63] For the southern backthrust, 76% of model elements are consistent with triggering by only the change in normal stress. This percentage is matched using CFS when μ' equals 0.8. However, again the percentages increase with increased μ' until they level off at a μ' of 1.4 where 81% of model elements are consistent with stress triggering.

[64] The correspondence between afterslip and unclamping indicates that μ' is high for these structures, at least 0.8. In both cases slip corresponds with unclamping to a degree beyond that expected by a CFS model of slip triggering. This may indicate that our measure of stress triggering is too simple. For example we assume that the backthrusts respond only to stress changes from the earthquake, we have not included any prestress or stress changes from postseismic processes. It may also indicate that another process is dominating over CFS triggering to allow the propagation of slow slip.

[65] The correspondence between the patterns of unclamping and afterslip on the backthrusts does not hold for seismic slip on the southern backthrust. The stress changes on the southern backthrust caused by coseismic slip from only the main plane are calculated and compared to the coseismic slip pattern on the southern backthrust (Figure 10). In this case the normal stress change pattern does not correlate with slip at all, but a better match is found with the shear stress changes. This could indicate that different mechanisms are responsible for nucleating and/or propagating slip in velocity-weakening (seismic slip) versus velocity-strengthening (slow slip) frictional environments. However, if the slip on the southern backthrust is coseismic, then comparing it to the static stress changes from rupture on the main plane is not strictly appropriate. Dynamic stresses are usually orders of magnitude larger than static stress changes and are generally

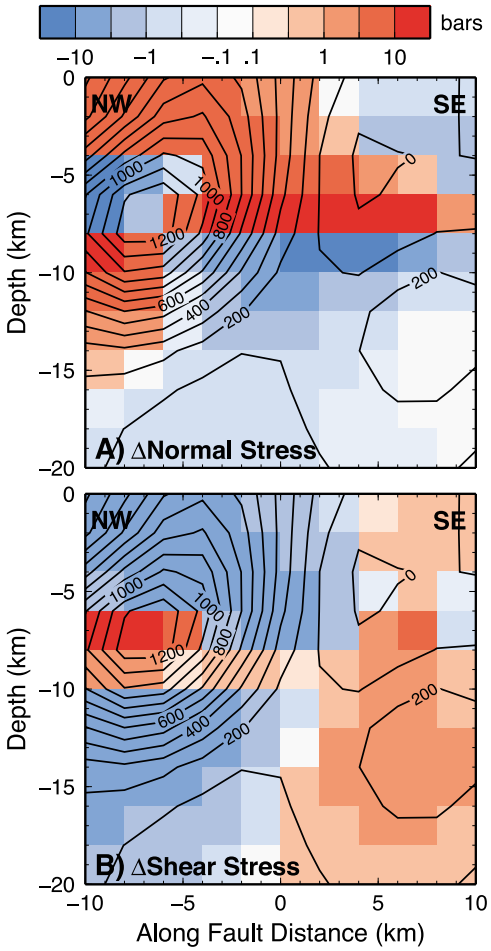

Figure 10. (a) Normal and (b) shear stress changes for dip slip on the southern backthrust structure caused by coseismic slip on only the main rupture plane and compared to coseismic slip on the southern backthrust (contours in mm). Gridding for the stress change calculation is identical to slip model gridding.

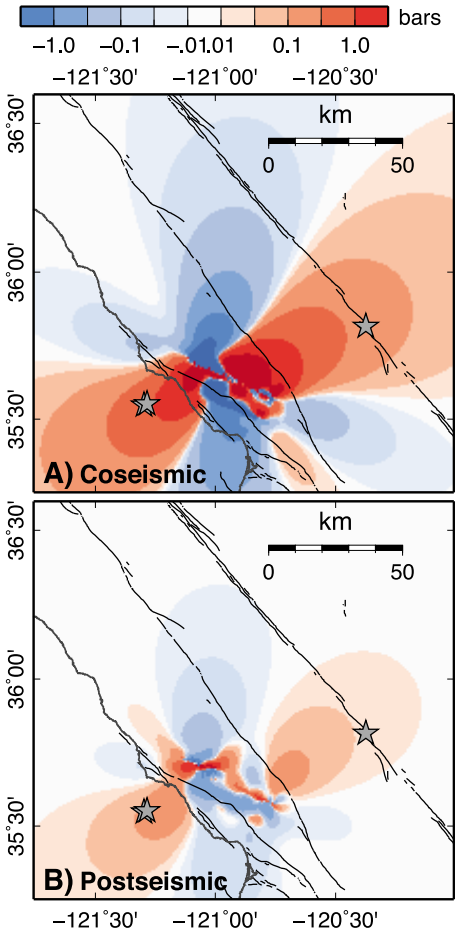

Figure 11. ΔCFS on planes aligned with the San Andreas fault, with strike = −41°, dip = 90°, rake = 180°, and $\mu' = 0.4$ and calculated at depth = 8 km. (a) Coseismic portion of $C_{mb_s} P^{exp}_{mb_s} P_{mb_n}$ model. (b) Postseismic portion of $C_{mb_s} P^{exp}_{mb_s} P_{mb_n}$ model.

responsible for propagating coseismic rupture onto secondary structures [*Harris et al.*, 1991]. Our data contain no information about the rupture history, nor are we attempting to calculate dynamic stresses. Nonetheless, the patterns of static and maximum dynamic stress can be similar, with differences related mostly to rupture directivity [*Kilb et al.*, 2000]). The SSEQ was a unilateral rupture, with slip occurring only to the southeast of the hypocenter [e.g., *Ji et al.*, 2004]. Directivity would have magnified dynamic stresses on the southern backthrust.

[66] The calculated stress changes are also dependent on the orientation for which they are calculated. Stress changes on planes with steeper and gentler dips than determined by *McLaren et al.* [2008] were also calculated. For the northern backthrust, stress changes on a plane with steeper dip (75°) provide a somewhat better correspondence with slip than for a plane with 60° dip. While the slip still corresponds strongly with unclamping only (90% of elements are consistent), 85% of elements are consistent with a μ' of 0.8 (Figure 9). Although a slip inversion with a steeper northern backthrust provides a worse fit to the data, *McLaren et al.* [2008] found that the aftershocks in this area show an apparent change in dip from 45° in the northwest to 70° in the southeast, where the slip is concentrated. The improved correspondence between stress change and slip may indicate that this steeper dip is more correct. Neither a steeper nor a gentler dipping plane provides a stress change pattern on the southern backthrust that is more consistent with ΔCFS than the value of 32° used in our model inversion.

5.3. Stress Changes at Parkfield

[67] To investigate the effect of the SSEQ on the Parkfield segment, we calculate stress changes in the orientation and slip direction of the San Andreas fault from our final slip model ($C_{mb_s} P^{exp}_{mb_s} P_{mb_n}$). We calculate ΔCFS (equation 11) on the Parkfield segment with μ' equal to 0.4; a value used for the Parkfield segment by previous authors studying triggered microseismicity [*Toda and Stein*, 2002].

[68] The PKEQ, as well two northwest-striking right-lateral SSEQ aftershocks occurred where future earthquakes were encouraged by the change in CFS (Figure 11). In fact, CFS was increased by the SSEQ throughout the Parkfield segment. Futhermore, among the diverse aftershock focal mechanisms, *McLaren et al.* [2008] find strike-slip events near the Rinconada fault to the southeast of the rupture zone, where we calculate that SAF oriented strike-slip earthquakes would be encouraged.

[69] The 2004 earthquake departed from the pattern established by the previous events by nucleating in the southeast. The 1966 Parkfield earthquake's hypocenter was located northwest of the town of Parkfield and rupture propagated southward. The hypocentral areas of both the 1966 and the 2004 Parkfield earthquakes experienced increased CFS from 0.1 to 0.25 bars from the combined coseismic and postseismic slip (Figure 12). Small changes, but nonetheless amounts that have been observed to correlate with increased seismicity [*King et al.*, 1994; *Hardebeck et al.*, 1998; *Toda et al.*, 1998]. Interestingly, the 2004 hypocenter occurred on the southeast end of the Parkfield segment, near the maximum shear stress increase (0.1–0.14 bars), rather than to the northwest near the 1966 hypocenter where the fault still experienced increased shear stresses, but of an order of magnitude less (0.02–0.03 bars). We note that while there was no discernible effect on shallow microseismicity along the SAF following the SSEQ [*Aron and Hardebeck*, 2009], *Nadeau and Guilhem* [2009] report that the rate of nonvolcanic tremor on a ~25-km-deep section of the SAF was enhanced below the 2004 hypocenter, where shear stress increases were maximum. The increased tremor may reflect accelerated deep shear on the SAF that further increased the load on the overlying SAF prior to the Parkfield earthquake.

[70] There is a slight correspondence between fault unclamping (positive change in normal stress) and peak slip in the 2004 earthquake. However, given that the location of peak slip in the 2004 Parkfield earthquake is very near the location of peak slip in the 1934 earthquake [*Segall and Du*, 1993], it is likely that it is controlled more by persistent features of the Parkfield segment, such as heterogeneously distributed fault frictional parameters. Peak afterslip following the Parkfield earthquake also occurred to the northwest, near the peak in unclamping from the SSEQ. However, this may again be more a function of the distribution of fault frictional parameters rather than a reaction to the SSEQ stress changes.

[71] Our choices regarding the SSEQ distributed slip model do not strongly affect the stress changes on the Parkfield

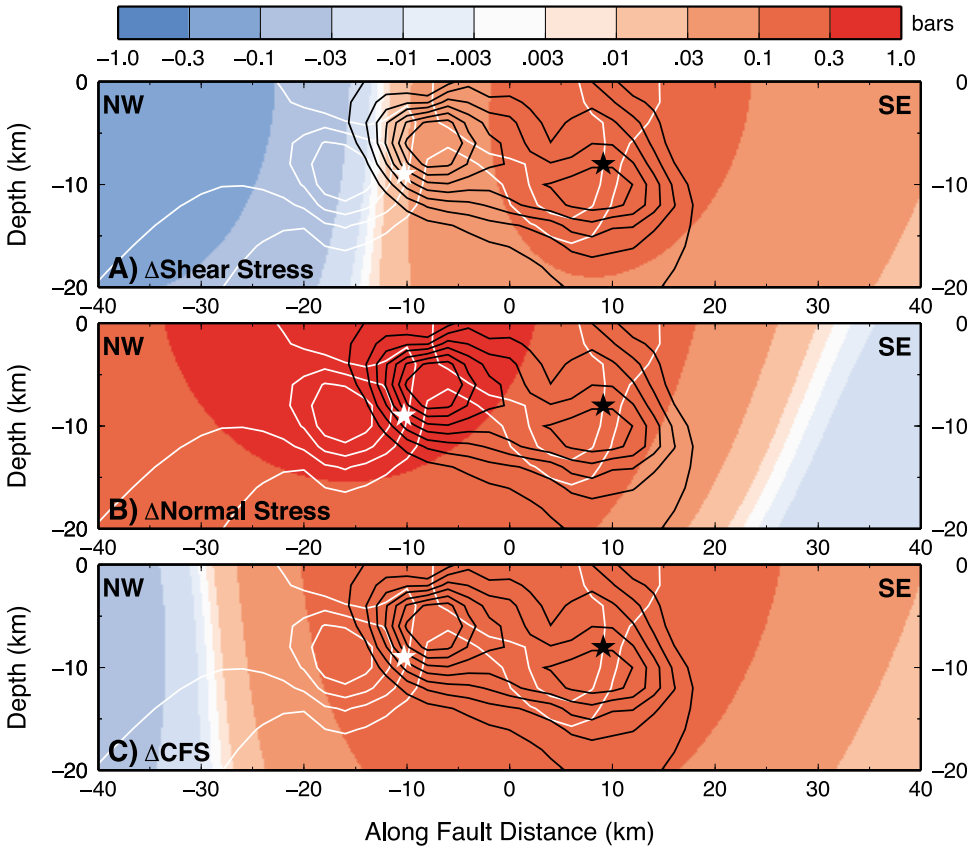

Figure 12. Stress changes along the Parkfield segment of the San Andreas fault for planes with strike = −41°, dip = 90°, and rake = 180° from coseismic portion of the $C_{mb_s} P_{mb_s}^{exp} P_{mb_n}$ model. (a) Right-lateral strike-slip shear stress change. (b) Normal stress changes, positive is unclamping. (c) ΔCFS with μ' = 0.4. In all plots black contours show coseismic slip in the 2004 Parkfield earthquake and white contours show postseismic afterslip from the Parkfield earthquake [*Johanson et al.*, 2006]. Both sets of contours have 50 mm intervals and the outermost contour is for 50 mm. The black star marks the location of the 2004 Parkfield earthquake's hypocenter and the white star is the location of the 1966 hypocenter.

segment. The Parkfield segment is far enough away from the San Simeon rupture that the details of the slip distribution are not very important for the calculated stress changes. Instead, the locations of the stress change lobes are controlled most by the locations and strike directions of the model fault planes. In our model, the main plane and the southern backthrust have similar strikes, leading to similar stress change patterns for models with and without coseismic slip on the southern back thrust.

[72] Because of the strong dependence on model geometry, the postseismic stress changes have a similar pattern to the coseismic (Figure 13). Though the shallow postseismic slip acts to encourage the PKEQ, it does not produce stresses greater than the 0.1 bars earthquake triggering threshold.

6. Conclusions

[73] We performed inversions for distributed slip during the San Simeon earthquake under several scenarios to determine whether slip may have occurred on two structures subconjugate to the coseismic rupture plane. We found that the data are well fit by a model including decaying postseismic slip on the main rupture plane and the southern back thrust. However, both postseismic interferograms could not be fit by a single slip distribution undergoing exponential decay. Allowing for enhanced early slip on the main plane and possibly on the northern backthrust improves the fit to interferograms A, B, and mostly C. Overall, the postseismic moment release was 14% of that from coseismic slip; however, this is a lower bound. The patterns of postseismic slip on the backthrust structures match the patterns of unclamping produced by the coseismic slip. No value for μ' below 1.0 results in a ΔCFS field that matches the aseismic slip distributions better than the normal stress alone.

[74] The data strongly favor coseismic slip on the southern backthrust, in addition to the northeast-dipping Oceanic fault. However, the GPS data provide our best constraint on coseismic-only deformation and even they may contain portions of early postseismic motion. If the slip on the southern backthrust were in fact postseismic, it would have to have occurred within days following the SSEQ. Data sources with a better separation between coseismic and postseismic slip, such as seismic data, might be better able to address whether this slip is truly coseismic.

[75] Coseismic slip from the San Simeon earthquake produced static ΔCFS encouraging right-lateral strike slip throughout the Parkfield segment. In fact, the maximum ΔCFS along the San Andreas fault was on the Parkfield

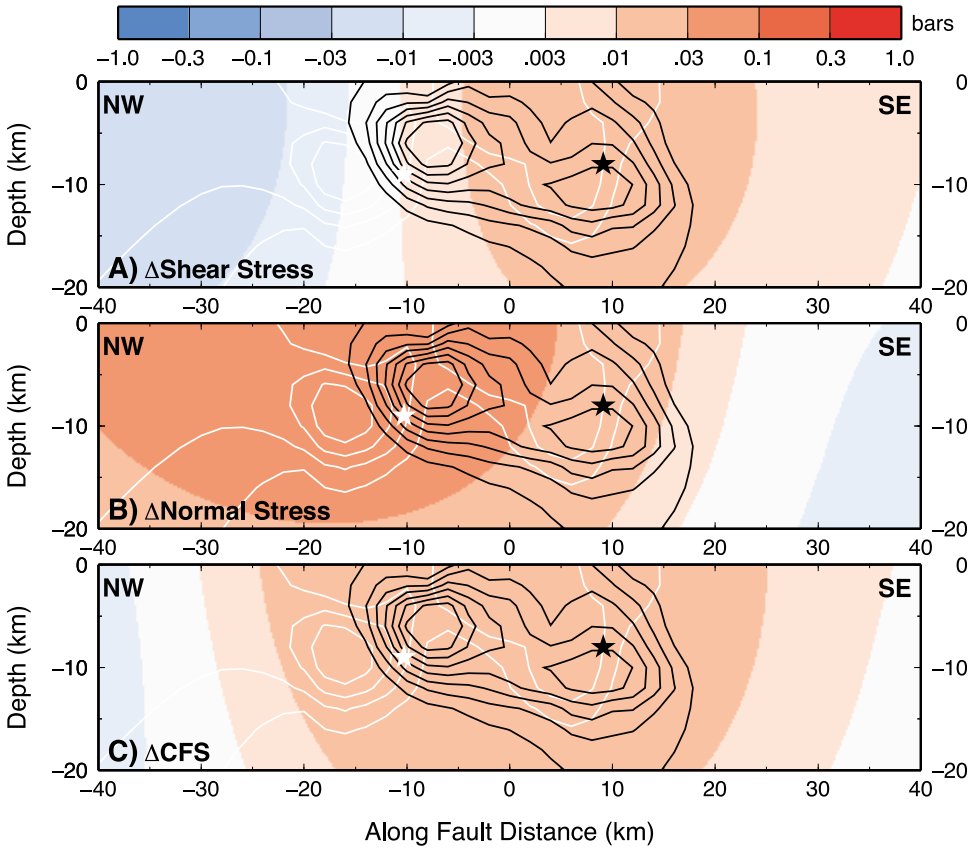

Figure 13. Same as Figure 12 for the postseismic portion of the model. (a) Right-lateral strike-slip shear stress change. (b) Normal stress changes, positive is unclamping. (c) ΔCFS with $\mu' = 0.4$. Notations are the same as in Figure 12.

segment. While the ΔCFS at the hypocenters of the 2004 and 1966 Parkfield earthquakes were similar, the nucleation site of the 2004 earthquake experienced about 10 times greater increase in shear stress than that of the 1966 earthquake. Postseismic slip further increased coulomb stress at the site of the 2004 Parkfield earthquake in a similar pattern to the coseismic but were an order of magnitude smaller than the coseismic stress changes.

[76] Decreased stress in the northwest end of the Parkfield segment due to the 1983 Coalinga-Nuñez earthquakes [*Toda and Stein*, 2002] and due to the 1993–1996 slow slip event [*Murray and Segall*, 2005] and accompanying earthquakes [*Nadeau and McEvilly*, 1999], together with the increased shear stress to the southeast from coseismic and postseismic slip in the San Simeon earthquake may have converged to favor the southern Parkfield segment, over the northern, as the nucleation site for the 2004 event.

[77] **Acknowledgments.** This work was supported by NASA under award NNX08A6506 and by the USGS Mendenhall Fellowship program. Our thanks to Charles W. Wicks for providing the RADARSAT interferogram. BSL contribution 10-03.

References

Aron, A., and J. Hardebeck (2009), Seismicity rate changes along the central California coast due to stress changes from the 2003 M6.5 San Simeon and 2004 M6.0 Parkfield earthquakes, *Bull. Seismol. Soc. Am.*, *99*(4), 2280–2292.

Bakun, W. H., and A. G. Lindh (1985), The Parkfield, California, earthquake prediction experiment, *Science*, *229*(4714), 619–624.

Bakun, W. H., and T. V. McEvilly (1979), Earthquakes near Parkfield, California: Comparing the 1934 and 1966 sequences, *Science*, *205*(4413), 1375–1377.

Bakun, W. H., and T. V. McEvilly (1984), Recurrence models and Parkfield, California, earthquakes, *J. Geophys. Res.*, *89*(5), 3051–3058.

Bakun, W. H., et al. (2005), Implications for prediction and hazard assessment from the 2004 Parkfield earthquake, *Nature*, *437*(7061), 969–974.

Ben-Zion, Y., J. R. Rice, and R. Dmowska (1993), Interaction of the San Andreas fault creeping segment with adjacent great rupture zones and earthquake recurrence at Parkfield, *J. Geophys. Res.*, *98*(B2), 2135–2144.

Bürgmann, R., P. A. Rosen, and E. J. Fielding (2000), Synthetic aperture radar interferometry to measure Earth's surface topography and its deformation, *Annu. Rev. Earth Planet. Sci.*, *28*, 169–209.

Byerlee, J. (1978), Friction of rocks, *Pure Appl. Geophys.*, *116*(4–5), 615–626.

Donnellan, A., and G. A. Lyzenga (1998), GPS observations of fault afterslip and upper crustal deformation following the northridge earthquake, *J. Geophys. Res.*, *103*(B9), 21,285–21,297.

Feigl, K. L., et al. (1993), Space geodetic measurement of crustal deformation in central and southern California, 1984–1992, *J. Geophys. Res.*, *98*(B12), 21,677–21,712.

Freed, A. M., and L. Jin (2001), Delayed triggering of the 1999 Hector Mine earthquake by viscoelastic stress transfer, *Nature*, *411*(6834), 180–183.

Gwyther, R. L., M. T. Gladwin, M. Mee, and R. H. G. Hart (1996), Anomalous shear strain at Parkfield during 1993–94, *Geophys. Res. Lett.*, *23*(18), 2425–2428.

Hardebeck, J. L., J. J. Nazareth, and E. Hauksson (1998), The static stress change triggering model; constraints from two southern California aftershock sequences, *J. Geophys. Res.*, *103*(B10), 24,427–24,437.

Hardebeck, J. L., et al. (2004), Preliminary report on the 22 December 2003, M6.5 San Simeon, California earthquake, *Seismol. Res. Lett.*, *75*(2), 155–172.

Harris, R. A. (1998), Introduction to special section: Stress triggers, stress shadows, and implications for seismic hazard, *J. Geophys. Res.*, *103*(B10), 24,347–24,358.

Harris, R. A., and R. W. Simpson (2002), The 1999 M_w7.1 Hector Mine, California, earthquake: A test of the stress shadow hypothesis?, *Bull. Seismol. Soc. Am.*, *92*(4), 1497–1512.

Harris, R. A., R. J. Archuleta, and S. M. Day (1991), Fault steps and the dynamic rupture process; 2-D numerical simulations of a spontaneously propagating shear fracture, *Geophys. Res. Lett.*, *18*(5), 893–896.

Hauksson, E., D. Oppenheimer, and T. M. Brocher (2004), Imaging the source region of the 2003 San Simeon earthquake within the weak Franciscan subduction complex, central California, *Geophys. Res. Lett.*, *31*, L20607, doi:10.1029/2004GL021049.

Hearn, E. H., R. Bürgmann, and R. E. Reilinger (2002), Dynamics of Izmit earthquake postseismic deformation and loading of the Duzce earthquake hypocenter, *Bull. Seismol. Soc. Am.*, *92*(1), 172–193.

Helmberger, D. V., P. G. Somerville, and E. Garnero (1992), The location and source parameters of the Lompoc, California, earthquake of 4 November 1927, *Bull. Seismol. Soc. Am.*, *82*(4), 1678–1709.

Ji, C., K. L. Larson, Y. Tan, K. W. Hudnut, and K. Choi (2004), Slip history of 2003 San Simeon earthquake constrained by combining 1-hz GPS, strong motion, and teleseismic data, *Geophys. Res. Lett.*, *31*, L17608, doi:10.1029/2004GL020448.

Johanson, I. A., E. J. Fielding, F. Rolandone, and R. Bürgmann (2006), Coseismic and postseismic slip of the 2004 Parkfield earthquake from space-geodetic data, *Bull. Seismol. Soc. Am.*, *96*(4B), S269–S282.

Jonsson, S., H. Zebker, P. Segall, and F. Amelung (2002), Fault slip distribution of the 1999 M_w 7.1 Hector Mine, California, earthquake, estimated from satellite radar and GPS measurements, *Bull. Seismol. Soc. Am.*, *92*(4), 1377–1389.

Kilb, D., J. Gomberg, and P. Bodin (2000), Triggering of earthquake aftershocks by dynamic stresses, *Nature*, *408*(6812), 570–574.

King, G. C. P., R. S. Stein, and L. Jian (1994), Static stress changes and the triggering of earthquakes, *Bull. Seismol. Soc. Am.*, *84*(3), 935–953.

Langbein, J., R. L. Gwyther, R. H. Hart, and M. T. Gladwin (1999), Slip-rate increase at Parkfield in 1993 detected by high-precision EDM and borehole tensor strainmeters, *Geophys. Res. Lett.*, *26*(16), 2529–2532.

Langbein, J., et al. (2005), Preliminary report on the 28 September 2004, M6.0 Parkfield, California earthquake, *Seismol. Res. Lett.*, *76*, 10–26.

Langbein, J., J. R. Murray, H. A. Snyder, R. A. Harris, and J. R. Arrowsmith (2006), Coseismic and initial postseismic deformation from the 2004 Parkfield, California, earthquake, observed by global positioning system, electronic distance meter, creepmeters, and borehole strainmeters, *Bull. Seismol. Soc. Am.*, *96*(4B), S304–S320.

Lettis, W. R., K. L. Hanson, J. R. Unruh, M. K. McLaren, and W. U. Savage (2004), Quaternary tectonic setting of south-central coastal California, *U.S. Geol. Surv. Bull., 1999-AA*, 24 pp.

McLaren, M. K., J. L. Hardebeck, N. van der Elst, J. R. Unruh, G. W. Bawden, and J. L. Blair (2008), Complex faulting associated with the 22 December 2003 M_w6.5 San Simeon, California, earthquake, aftershocks, and post-seismic surface deformation, *Bull. Seismol. Soc. Am.*, *98*(4), 1659–1680.

Murray, J., and P. Segall (2005), Spatiotemporal evolution of a transient slip event on the San Andreas fault near Parkfield, California, *J. Geophys. Res.*, *110*, B09407, doi:10.1029/2005JB003651.

Murray, J., J. Langbein, R. A. Harris, and J. R. Arrowsmith (2006), Slip on the San Andreas fault at Parkfield, California, over two earthquake cycles, and the implications for seismic hazard, *Bull. Seismol. Soc. Am.*, *96*(4B), S283–S303.

Nadeau, R., and A. Guilhem (2009), Nonvolcanic tremor evolution and the San Simeon and Parkfield, California, earthquakes, *Science*, *325*(5937), 191–193.

Nadeau, R. M., and T. V. McEvilly (1999), Fault slip rates at depth from recurrence intervals of repeating microearthquakes, *Science*, *285*(5428), 718–721.

Okada, Y. (1985), Surface deformation due to shear and tensile faults in a half-space, *Bull. Seismol. Soc. Am.*, *75*(4), 1135–1154.

Parsons, T. E., and D. S. Dreger (2000), Static-stress impact of the 1992 Landers earthquake sequence on nucleation and slip at the site of the 1999 M7.1 Hector Mine earthquake, southern California, *Geophys. Res. Lett.*, *27*(13), 1949–1952.

Parsons, T. E., R. S. Stein, R. W. Simpson, and P. A. Reasenberg (1999), Stress sensitivity of fault seismicity; a comparison between limited-offset oblique and major strike-slip faults, *J. Geophys. Res.*, *104*(B9), 20,183–20,202.

Perfettini, H., R. S. Stein, R. W. Simpson, and M. Cocco (1999), Stress transfer by the 1988–1989 M5.3 and 5.4 Lake Elsman foreshocks to the Loma Prieta fault; unclamping at the site of peak mainshock slip, *J. Geophys. Res.*, *104*(B9), 20,169–20,182.

Pollitz, F. F., and I. S. Sacks (2002), Stress triggering of the 1999 Hector Mine earthquake by transient deformation following the 1992 Landers earthquake, *Bull. Seismol. Soc. Am.*, *92*(4), 1487–1496.

Price, E. J., and R. Burgmann (2002), Interactions between the Landers and Hector Mine, California, earthquakes from space geodesy, boundary element modeling, and time-dependent friction, *Bull. Seismol. Soc. Am.*, *92*(4), 1450–1469.

Rolandone, F., D. Dreger, M. Murray, and R. Bürgmann (2006), Coseismic slip distribution of the 2003 M_w6.6 San Simeon earthquake, California, determined from GPS measurements and seismic waveform data, *Geophys. Res. Lett.*, *33*, L16315, doi:10.1029/2006GL027079.

Rolandone, F., R. Burgmann, D. C. Agnew, I. A. Johanson, D. C. Templeton, M. A. d'Alessio, S. J. Titus, C. DeMets, and B. Tikoff (2008), Aseismic slip and fault-normal strain along the central creeping section of the San Andreas fault, *Geophys. Res. Lett.*, *35*, L14305, doi:10.1029/2008GL034437.

Savage, J. C., J. L. Svarc, and W. H. Prescott (2003), Near-field postseismic deformation associated with the 1992 Landers and 1999 Hector Mine, California, earthquakes, *J. Geophys. Res.*, *108*(B9), 2432, doi:10.1029/2002JB002330.

Savage, J. C., J. L. Svarc, and S. Yu (2005), Postseismic relaxation and transient creep, *J. Geophys. Res.*, *110*, B11402, doi:10.1029/2005JB003687.

Savage, J. C., J. L. Svarc, and S.-B. Yu (2007), Postseismic relaxation and aftershocks, *J. Geophys. Res.*, *112*, B06406, doi:10.1029/2006JB004584.

Segall, P., and Y. Du (1993), How similar were the 1934 and 1966 Parkfield earthquakes?, *J. Geophys. Res.*, *98*(B3), 4527–4538.

Segall, P., R. Burgmann, and M. Matthews (2000), Time-dependent triggered afterslip following the 1989 Loma Prieta earthquake, *J. Geophys. Res.*, *105*(B3), 5615–5634.

Shen, Z.-k., and D. D. Jackson (1993), Global positioning system reoccupation of early triangulation sites: Tectonic deformation of the southern coast ranges, *J. Geophys. Res.*, *98*(B6), 9931–9946.

Stark, P. B., and R. L. Parker (1995), Bounded-variable least-squares - An algorithm and applications, *Comput. Stat.*, *10*(2), 129–141.

Stein, R. S. (1999), The role of stress transfer in earthquake occurrence, *Nature*, *402*(6762), 605–609.

Stein, R. S., G. King, and J. Lin (1994), Stress triggering of the 1994 M6.7 Northridge, California, earthquake by its predecessors, *Science*, *265*(5177), 1432–1435.

Stein, R. S., A. A. Barka, and J. H. Dieterich (1997), Progressive failure on the North Anatolian fault since 1939 by earthquake stress triggering, *Geophys. J. Int.*, *128*(3), 594–604.

Stein, S. A., and R. G. Gordon (1984), Statistical tests of additional plate boundaries from plate motion, *Earth Planet. Sci. Lett.*, *69*(2), 401–412.

Thomas, A. L. (1993), Poly3D: A three-dimensional, polygonal element, displacement discontinuity boundary element computer program with applications to fracture, faults, and cavities in the Earth's crust, M.S. thesis, Stanford Univ., Stanford, Calif.

Titus, S. J., C. DeMets, and B. Tikoff (2005), New slip rate estimates for the creeping segment of the San Andreas fault, California, *Geology*, *33*(3), 205–208.

Toda, S., and R. S. Stein (2002), Response of the San Andreas fault to the 1983 Coalinga-Nuñez earthquakes: An application of interaction-based probabilities for Parkfield, *J. Geophys. Res.*, *107*(B6), 2126, doi:10.1029/2001JB000172.

Toda, S., R. S. Stein, P. A. Reasenberg, J. H. Dieterich, and A. Yoshida (1998), Stress transferred by the 1995 M_w6.9 Kobe, Japan, shock: Effect on aftershocks and future earthquake probabilities, *J. Geophys. Res.*, *103*(B10), 24,543–24,565.

Toppozada, T. R., D. L. Parke, and C. T. Higgins (1978), Seismicity of California: 1900–1931, *Spec. Rep. 135*, 39 pp., Calif. Div. of Mines and Geol., Sacremento.

R. Bürgmann and I. A. Johanson, Berkeley Seismological Laboratory, University of California, 215 McCone Hall, Berkeley, CA 94720, USA. (ingrid@seismo.berkeley.edu)